Accepted Manuscript

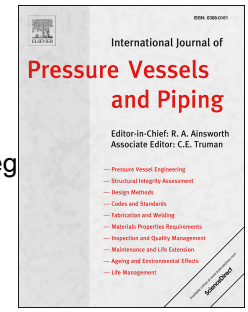

Effects of thermal gradient on failure of a thermoplastic composite pipe (TCP) riser leg

James C. Hastie, Igor A. Guz, Maria Kashtalyan

PII: S0308-0161(18)30525-8

DOI: https://doi.org/10.1016/j.ijpvp.2019.03.027

Reference: IPVP 3877

To appear in: *International Journal of Pressure Vessels and Piping*

Received Date: 30 November 2018

Revised Date: 28 January 2019

Accepted Date: 20 March 2019

Please cite this article as: Hastie JC, Guz IA, Kashtalyan M, Effects of thermal gradient on failure of a thermoplastic composite pipe (TCP) riser leg, *International Journal of Pressure Vessels and Piping* (2019), doi: https://doi.org/10.1016/j.ijpvp.2019.03.027.

Effects of Thermal Gradient on Failure of a Thermoplastic Composite Pipe (TCP) Riser Leg

James C. Hastie*, Igor A. Guz, Maria Kashtalyan

School of Engineering, University of Aberdeen, Scotland, UK
Centre for Micro- and Nanomechanics (CEMINACS)
**Corresponding author. Email: r03jh15@abdn.ac.uk*

Effects of Thermal Gradient on Failure of a Thermoplastic Composite Pipe (TCP) Riser Leg

Abstract

Thermoplastic composite pipe (TCP), consisting of a fibre-reinforced thermoplastic laminate fully bonded between homogeneous thermoplastic liners, is an ideal candidate to replace traditional steel riser pipes in deepwater where high specific strengths and moduli and corrosion resistance are advantageous. During operation, risers are subjected to combined mechanical and thermal loads. In the present paper, a 3D finite element (FE) model is developed to analyse stress state in a section of TCP under combined pressure, axial tension and thermal gradient, illustrative of a single-leg hybrid riser (SLHR) application. From the obtained stresses, through-thickness failure coefficient is evaluated based on appropriate failure criteria. The effects of increasing the internal-to-external thermal gradient are investigated considering temperature dependent material properties. The influence of varying the thickness of the isotropic liners with respect to the laminate is examined.

Keywords: Thermoplastic composite pipe; composite riser; thermal gradient

1. Introduction

Fibre-reinforced plastic (FRP) materials have been viewed as candidates to replace steels in deepwater exploration and production (E&P) applications for a number of advantages including high specific strengths and moduli and excellent corrosion resistance. Thermoplastic composite pipe (TCP) is an example of an FRP product attracting growing interest in the offshore E&P sector. TCP consists of a fibre-reinforced thermoplastic multi-ply laminate with inner and outer homogeneous thermoplastic liners, which provide fluid tightness and wear resistance. Figure 1 shows the basic construction. Polyethylene (PE), polyamide (PA) and polyetheretherketone (PEEK) thermoplastics are used, superior to thermosets in terms of ductility, toughness, impact resistance and stability at extreme temperatures. The thermoplastic is reinforced with tape- or filament-wound (FW) carbon, glass or aramid fibres to form the laminate. A melt-fusion process typified by leading manufacturers is used to fully bond all layers.

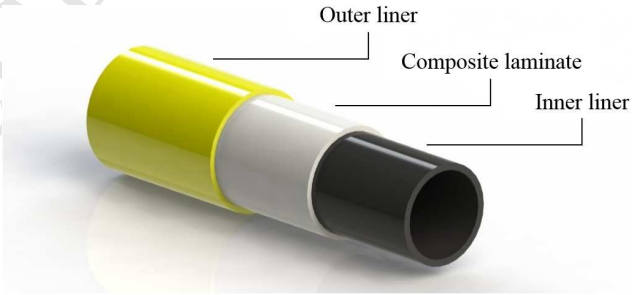

Figure 1. TCP configuration

The behaviour of multi-layered, fibre-reinforced pipes under mechanical loads for practical application has been studied for several decades (see reviews in [1,2]). The response of thermoplastic-based pipe of the tri-layer TCP construction specifically, often referred to in different sources as ‘reinforced thermoplastic pipe (RTP)’, under various discrete and combined mechanical loads relevant to subsea applications has also been studied in recent literature. Bai et al. [3] investigated external pressure

collapse of TCP consisting of aramid fibre and high-density polyethylene (HDPE) layers by theoretical, finite element (FE) and experimental methods. Kruijer et al. [4] investigated the behaviour of pressurised TCP considering slack of non-impregnated aramid reinforcement cords. Ashraf et al. [5] used FE modelling to investigate bending-induced buckling of carbon/PEEK TCP. Bending of aramid/PE TCP was investigated numerically by Yu et al. [6], accounting for strain-dependent nonlinearity. The behaviour of TCP under combined pressure and bending [7], pressure-tension [8] and bending-tension [9] has been studied largely by numerical means. Variations of TCP have been developed and studied, including multi-layered plastic pipes reinforced with steel wires or strips as an alternative to, or in conjunction with, non-metallic fibres [10,11]. Weight added by steel can improve stability for certain subsea piping systems.

In addition to mechanical loads, subsea tubulars are subjected to uniform temperature change (e.g. deploying into cool seawater) and thermal gradients during operation (i.e. resulting from the mismatch between hot internal fluids and external seawater). Literature pertaining to FRP and multi-layered pipes under thermomechanical load is less widely available. Xia et al. [12] presented an elastic solution based on classical lamination theory for pressurised sandwich pipes with isotropic core and orthotropic skins subjected to temperature change. Akçay and Kaynak [13] used analytical expressions to investigate failure of multi-layered FRP cylinders under pressure and uniform thermal load for plane-strain and closed-end conditions. A 3D elasticity solution for multi-layered FW pipes subjected to internal pressure and temperature gradient was presented by Bakaiyan et al. [14]. A closed-form stress solution for pressurised vessels with multiple isotropic layers subjected to thermal load was presented by Zhang et al. [15]. Wang et al. [16] proposed a strategy for predicting failure of a carbon/epoxy vessel under pressure and thermal loading based on material property degradation and micromechanics of failure (MMF) criterion. Analytical solutions for stresses and displacements in heated and pressurised multi-layered pipes were developed by Vedeld and Sollund [17] and Sollund et al. [18]. The solution of Vedeld and Sollund [17], which assumed uniform temperature distribution within each layer, was subsequently refined by Yeo et al. [19], who found their refined solution to produce more accurate predictions than the original.

In general, literature on thermal loading of composite pipes has largely been limited to analytical studies. A numerical model, developed for example in dedicated FE software packages such as Abaqus or ANSYS, would allow a wide array of mechanical and thermal load combinations to be studied. Furthermore, defects such as delamination can be introduced where this may prove analytically complex or unfeasible.

As well as a requirement for greater overall understanding of the behaviour of composite pipes such as TCP under thermal load, there is a particular need for investigating behaviour when accounting for the temperature dependence of material properties. Composite properties are most often taken to be constant in existing literature, likely a by-product of the lack of available data to fully define a material over an appropriate temperature range. To more accurately predict stress and strain states and resulting failure it is crucial that temperature dependence is accounted for.

In the present paper, the problem of TCP under combined pressure, axial tension and thermal gradient illustrative of a deepwater riser application is considered. A 3D FE model is developed for predicting stress state under the combined loading taking into account temperature dependent carbon/PEEK material properties uniquely compiled and extrapolated from literature. From obtained stress distributions, through-thickness failure coefficients according to von Mises criterion for isotropic liners and Maximum Stress and Tsai-Hill criteria for orthotropic laminate are analysed. The effects of increasing the internal-to-external thermal gradient on failure are investigated. The influence of varying liner thickness with respect to the central laminate is also examined.

2. Problem Formulation

A single-leg hybrid riser (SLHR) system, illustrated in Figure 2, is an application in which the benefits of TCP can be exploited to great economic effect. The riser leg, tensioned by buoyancy to avoid buckling, is isolated from vessel motions by a flexible jumper. Let us consider a section along the leg. During operation, the section is subjected to internal and external pressures (P_0 and P_a), axial tension (F_A), and internal and external surfaces temperatures (T_0 and T_a).

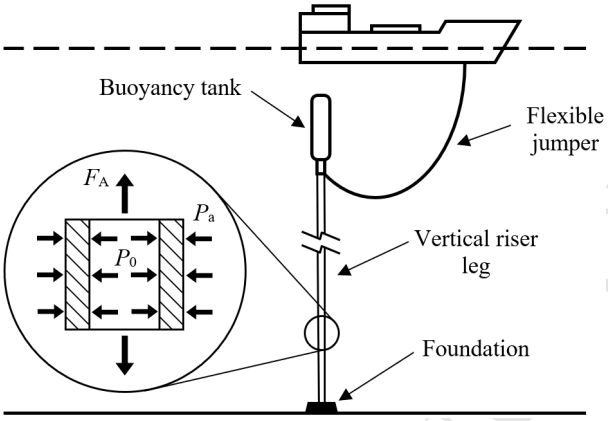

Figure 2. SLHR system

Here, we consider the section to be TCP with N layers as illustrated in Figure 3. Layers $k = 1$ and $k = N$ are isotropic liners and the remaining layers are orthotropic plies that together form the laminate. Under axisymmetric loading, stresses and strains are independent of the hoop coordinate, θ. Axial (z) and radial (r) displacements depend only on the corresponding directions i.e. [20]:

$$u_z = u_z(z), \quad u_\theta = u_\theta(r,z), \quad u_r = u_r(r), \tag{1}$$

where u_i denotes displacement in z, θ and r.

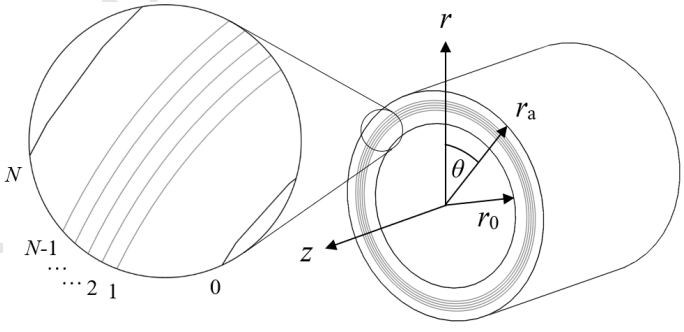

Figure 3. TCP in cylindrical coordinates

The strain-displacement relations are written as [20,21]:

$$\varepsilon_z^{(k)} = \frac{du_z^{(k)}}{dz} = \varepsilon_0, \quad \varepsilon_\theta^{(k)} = \frac{u_r^{(k)}}{r}, \quad \varepsilon_r^{(k)} = \frac{du_r^{(k)}}{dr},$$

$$\gamma_{\theta r}^{(k)} = \frac{du_\theta^{(k)}}{dr} - \frac{u_\theta^{(k)}}{r}, \quad \gamma_{zr}^{(k)} = 0, \quad \gamma_{z\theta}^{(k)} = \frac{du_\theta^{(k)}}{dz} = \gamma_0 r, \tag{2}$$

where γ_0 is a pipe twist per unit length and ε_0 is constant.

Layer stresses and strains in cylindrical coordinates are related by the constitutive equations [21]:

$$\begin{Bmatrix} \sigma_z \\ \sigma_\theta \\ \sigma_r \\ \tau_{\theta r} \\ \tau_{zr} \\ \tau_{z\theta} \end{Bmatrix}^{(k)} = \begin{bmatrix} \bar{C}_{11} & \bar{C}_{12} & \bar{C}_{13} & 0 & 0 & \bar{C}_{16} \\ \bar{C}_{12} & \bar{C}_{22} & \bar{C}_{23} & 0 & 0 & \bar{C}_{26} \\ \bar{C}_{13} & \bar{C}_{23} & \bar{C}_{33} & 0 & 0 & \bar{C}_{36} \\ 0 & 0 & 0 & \bar{C}_{44} & \bar{C}_{45} & 0 \\ 0 & 0 & 0 & \bar{C}_{45} & \bar{C}_{55} & 0 \\ \bar{C}_{16} & \bar{C}_{26} & \bar{C}_{36} & 0 & 0 & \bar{C}_{66} \end{bmatrix}^{(k)} \begin{Bmatrix} \varepsilon_z - \alpha_z \Delta T \\ \varepsilon_\theta - \alpha_\theta \Delta T \\ \varepsilon_r - \alpha_r \Delta T \\ \gamma_{\theta r} \\ \gamma_{zr} \\ \gamma_{z\theta} - 2\alpha_{z\theta} \Delta T \end{Bmatrix}^{(k)}, \tag{3}$$

where $\bar{C}_{ij}$ are the transformed stiffness constants corresponding to a fibre-reinforced layer orientated at angle φ, which describes the offset of the fibre longitudinal from the cylindrical z direction; α_z, α_θ, α_r and $\alpha_{z\theta}$ are the cylindrical coefficients of thermal expansion; ΔT is the change in temperature. The transformation of stiffness constants from material coordinates to off-axis directions is demonstrated in Appendix 1. Note that whilst the plies are orthotropic, the behaviour is strictly monotropic in relation to the global axis (i.e. fibre direction not aligned with z).

Under axisymmetric internal-to-external temperature differential, ΔT depends on the radial temperature distribution, $T(r)$:

$$\Delta T = T(r) - T_{\text{ref}}, \tag{4}$$

where T_{ref} is the initial (or reference) temperature.

The equation for steady-state heat conduction considering no heat generation for a multi-layered pipe in cylindrical coordinates is expressed as [14,15]:

$$\frac{\partial^2 T(r)}{\partial r^2} + \frac{1}{r}\frac{\partial T(r)}{\partial r} = 0. \tag{5}$$

Heat flux must satisfy continuity for layers $k = 1, 2, \ldots, N\text{-}1$:

$$q^{(k)}(r_k) = q^{(k+1)}(r_k), \tag{6}$$

where the heat flux through layer k with radial thermal conductivity λ_r (orthotropic λ_3) is obtained using Fourier's law:

$$q^{(k)} = -\lambda_r^{(k)} \frac{\partial T^{(k)}}{\partial r}. \tag{7}$$

Combining Equations (5) and (6) it can be shown that [15,22]:

$$\frac{T^{(k-1)}-T^{(k)}}{T^{(k)}-T^{(k+1)}}=\frac{\lambda_r^{(k+1)}}{\lambda_r^{(k)}}\frac{\ln\left(\frac{r^{(k)}}{r^{(k-1)}}\right)}{\ln\left(\frac{r^{(k+1)}}{r^{(k)}}\right)}. \tag{8}$$

The temperature at the interface between the *k*th and *k*+1th layer is deduced as [15]:

$$T^{(k)}=\frac{\lambda_r^{(k)}T^{(k-1)}\ln\left(\frac{r^{(k+1)}}{r^{(k)}}\right)+\lambda_r^{(k+1)}T^{(k+1)}\ln\left(\frac{r^{(k)}}{r^{(k-1)}}\right)}{\lambda_r^{(k)}\ln\left(\frac{r^{(k+1)}}{r^{(k)}}\right)+\lambda_r^{(k+1)}\ln\left(\frac{r^{(k)}}{r^{(k-1)}}\right)}. \tag{9}$$

Thus, the temperature at radius *r* in an arbitrary layer *k* is [15]:

$$T(r)=\frac{T^{(k)}-T^{(k-1)}}{\ln\left(\frac{r^{(k)}}{r^{(k-1)}}\right)}\ln\frac{r}{r^{(k)}}+T^{(k)}. \tag{10}$$

The distribution under uniform internal and external temperature is bound by:

$$T(r_0)=T_0,\quad T(r_\mathrm{a})=T_\mathrm{a}, \tag{11}$$

where r_0 and r_a are the inner and outer radius respectively.

The equilibrium equations for a long axisymmetric tube under prescribed loading are [20,21]:

$$\frac{d\sigma_r^{(k)}}{dr}+\frac{\sigma_r^{(k)}-\sigma_\theta^{(k)}}{r}=0, \tag{12a}$$

$$\frac{d\tau_{\theta r}^{(k)}}{dr}+\frac{2\tau_{\theta r}^{(k)}}{r}=0, \tag{12b}$$

$$\frac{d\tau_{zr}^{(k)}}{dr}+\frac{\tau_{zr}^{(k)}}{r}=0. \tag{12c}$$

From (12b) and (12c) we obtain:

$$\tau_{\theta r}^{(k)}=\frac{A^{(k)}}{r^2},\quad \tau_{zr}^{(k)}=\frac{B^{(k)}}{r}, \tag{13}$$

where $A^{(k)}$ and $B^{(k)}$ are unknown integration constants.

Combining the constitutive expressions (Equation (3)), equilibrium condition (12a), strain-displacement relations (2) and displacement field (1), one obtains a second-order ordinary differential equation of which the solution for isotropic and transversely isotropic layers is [21]:

$$u_r^{(k)}=D^{(k)}r+E^{(k)}r^{-1}, \tag{14}$$

where $D^{(k)}$ and $E^{(k)}$ are unknown constants.

Under internal and external pressure, the boundary conditions at inner and outer radii are written as [21]:

$$\sigma_r^{(1)}(r_0) = -P_0, \quad \sigma_r^{(N)}(r_a) = -P_a, \tag{15a}$$

$$\tau_{\theta r}^{(1)}(r_0) = \tau_{zr}^{(1)}(r_0) = 0, \quad \tau_{\theta r}^{(N)}(r_a) = \tau_{zr}^{(N)}(r_a) = 0. \tag{15b}$$

Assuming perfectly bonded layers, the interface continuities are [20]:

$$u_r^{(k)}(r_k) = u_r^{(k+1)}(r_k), \quad u_\theta^{(k)}(r_k) = u_\theta^{(k+1)}(r_k), \tag{16a}$$

$$\sigma_r^{(k)}(r_k) = \sigma_r^{(k+1)}(r_k), \quad \tau_{\theta r}^{(k)}(r_k) = \tau_{\theta r}^{(k+1)}(r_k), \quad \tau_{zr}^{(k)}(r_k) = \tau_{zr}^{(k+1)}(r_k). \tag{16b}$$

Axial force at the pipe end is determined by integrating σ_z over the cross-sectional area and torque by the moment of $\tau_{z\theta}$. Considering a long pipe subjected to tension, axial equilibrium and zero torsion are expressed by the integrals [21]:

$$2\pi \sum_{k=1}^{N} \int_{r_{k-1}}^{r_k} \sigma_z^{(k)}(r) r \, \mathrm{d}r = F_A, \tag{17a}$$

$$2\pi \sum_{k=1}^{N} \int_{r_{k-1}}^{r_k} \tau_{z\theta}^{(k)}(r) r^2 \, \mathrm{d}r = 0. \tag{17b}$$

By substituting Equations (15b) and (16b) into (13), $A^{(k)} = B^{(k)} = 0$. For N layers there exist $2N+2$ unknowns, i.e. $D^{(k)}$, $E^{(k)}$, ε_0 and γ_0 (for $k = 1, 2, \ldots, N$), that can be determined from boundary conditions, continuity conditions and axial/torque integrals in order to obtain displacements, stresses and strains.

3. Lamina Failure Criteria

For assessing local stress-based material failure, stresses must be transformed from cylindrical to principal material coordinates as follows [21]:

$$\begin{Bmatrix} \sigma_1 \\ \sigma_2 \\ \sigma_3 \\ \tau_{23} \\ \tau_{13} \\ \tau_{12} \end{Bmatrix} = \begin{bmatrix} m^2 & n^2 & 0 & 0 & 0 & 2mn \\ n^2 & m^2 & 0 & 0 & 0 & -2mn \\ 0 & 0 & 1 & 0 & 0 & 0 \\ 0 & 0 & 0 & m & -n & 0 \\ 0 & 0 & 0 & n & m & 0 \\ -mn & mn & 0 & 0 & 0 & m^2 - n^2 \end{bmatrix} \begin{Bmatrix} \sigma_z \\ \sigma_\theta \\ \sigma_r \\ \tau_{\theta r} \\ \tau_{zr} \\ \tau_{z\theta} \end{Bmatrix}, \tag{18}$$

where $m = \cos\varphi$ and $n = \sin\varphi$.

In this study, the Maximum Stress (herein "Max Stress") and Tsai-Hill criteria are compared. According to Max Stress, failure is assumed simply when the stress along a principal direction exceeds the corresponding allowable, i.e. when any of the following are exceeded:

$$-X_C < \sigma_1 < X_T, \quad -Y_C < \sigma_2 < Y_T, \quad -Z_C < \sigma_3 < Z_T,$$

$$|\tau_{23}| < Q, \quad |\tau_{13}| < R, \quad |\tau_{12}| < S, \tag{19}$$

where *X*, *Y* and *Z* are tensile or compressive strengths (subscripts 'T' and 'C') along directions 1, 2 and 3 respectively; *Q*, *R* and *S* are the shear strengths in coordinates 23, 13 and 12 respectively. Interaction amongst stresses within a lamina is unaccounted for, which can result in error for multi-axial cases. Stress interaction is accounted for in the widely used quadratic Tsai-Hill criterion, expressed as:

$$\frac{\sigma_1^2}{X_T^2}+\frac{\sigma_2^2}{Y_T^2}+\frac{\sigma_3^2}{Z_T^2}-\sigma_1\sigma_2\left(\frac{1}{X_T^2}+\frac{1}{Y_T^2}-\frac{1}{Z_T^2}\right)-\sigma_1\sigma_3\left(\frac{1}{X_T^2}-\frac{1}{Y_T^2}+\frac{1}{Z_T^2}\right)-\sigma_2\sigma_3\left(-\frac{1}{X_T^2}+\frac{1}{Y_T^2}+\frac{1}{Z_T^2}\right)+\frac{\tau_{23}^2}{Q^2}+\frac{\tau_{13}^2}{R^2}+\frac{\tau_{12}^2}{S^2}=1. \quad (20)$$

4. Numerical Simulation

4.1. TCP Mechanical Model

A 3D FE model was developed in Abaqus/CAE 2017 capable of predicting stress state in a section of TCP under combined pressures, tension and thermal gradient. Dimensions of the 'basic' configuration modelled for this study are given in Table 1. The inner liner, laminate and outer liner of the basic TCP are an equal thickness of 8mm, which we denote here as "8:8:8". In this study, the liner thicknesses are varied with respect to the laminate, for example 4:8:4 (equally thick liners), or 4:8:12 (unequal liners). The laminate is constructed of eight FW layers orientated in the sequence $[\pm 55]_4$, each wound to a thickness of 1mm.

Table 1. Basic TCP section dimensions

Dimension	**Value**
Inner radius, r_0 (mm)	76
Inner liner thickness, t_{in} (mm)	8
Laminate thickness, t_{lam} (mm)	8
Outer liner thickness, t_{out} (mm)	8
Outer radius, r_a (mm)	100

The TCP consists of unidirectional AS4/APC-2 carbon/PEEK laminate plies and homogeneous APC-2 PEEK liners. APC-2 PEEK composite has a glass transition temperature (T_g) of 143°C and can be used in lightly loaded applications at temperatures as high as 260°C [23]. Properties used to define the materials over a range of temperatures are given in Tables 2 and 3, where data has been carefully compiled as far as possible from literature. To the authors' best knowledge these tables represent the most comprehensive compilation of AS4/APC-2 properties over the relevant temperature range. Note that for practical application the designer should always assess properties of the specific chosen material experimentally. The following assumptions are made to fully define the AS4/APC-2 for temperature dependent analysis:

- Properties listed in Tables 2 and 3 are linearly inter/extrapolated over the temperature range considered in this study (which is below T_g).
- Poisson's ratio v_{23} at room temperature (RT) [26] is assumed to increase by 2.7% at 121°C as per reported data for v_{12} and v_{13} [25].
- Shear modulus G_{23} is calculated as:

$$G_{23}=\frac{E_2}{2(1+v_{23})}.$$

- Shear strength Q at RT [26] is assumed to reduce by 14.5% and 22.0% at 82°C and 121°C respectively as per reported data for R and S [23].
- It is assumed that thermal expansion coefficients remain unchanged over the temperature range investigated in this study.

Table 2. Unidirectional AS4/APC-2 properties

Property	**RT (23-24°C)**	**66°C**	**82°C**	**100°C**	**121°C**
E_1 (GPa) [24]	142	-	-	131	-
$E_2 = E_3$ (GPa) [24]	9.6	-	-	8.6	-
$G_{12} = G_{13}$ (GPa) [24]	6.0	-	-	4.8	-
G_{23} (GPa)	3.6*	-	-	3.2*	-
$v_{12} = v_{13}$ [25]	0.37	-	-	-	0.38
v_{23} [26]	0.33	-	-	-	0.34^{+}
α_1 (°C^{-1}) [26]	$-0.18\text{x}10^{-6}$	-	-	-	-
$\alpha_2 = \alpha_3$ (°C^{-1}) [26]	$23.94\text{x}10^{-6}$	-	-	-	-
λ_1 (Wm^{-1}°C^{-1}) [27]	4.0	4.35	4.5	4.60	4.8
$\lambda_2 = \lambda_3$ (Wm^{-1}°C^{-1}) [27]	0.43	0.46	0.48	0.50	0.53
X_T (MPa) [24]	2070	-	-	2008	-
$Y_T = Z_T$ (MPa) [24]	79	-	-	66	-
X_C (MPa) [28]	1234	1036	-	-	985
$Y_C = Z_C$ (MPa) [28]	176	163	-	-	136
Q (MPa) [26]	92	-	78.7^{+}	-	71.8^{+}
$R = S$ (MPa) [23]	186	-	159	-	145

*Calculated value; $^{+}$Estimated value

Table 3. Neat APC-2 PEEK properties

Property	**0°C**	**RT (23-24°C)**	**60°C**	**82°C**	**100°C**	**121°C**
E (GPa) [24]	-	4.1	-	3.8	-	3.5
v [24]	-	0.41	-	0.44	-	0.44
α (°C^{-1}) [24]	-	$50.8\text{x}10^{-6}$	-	-	-	-
λ (Wm^{-1}°C^{-1}) [29]	0.27	0.28	0.30	0.30	0.31	0.32
σ_y (MPa) [30]	119	106	76	-	51.77^{+}	-

$^{+}$Estimated value

Internal and external surface pressures are applied simultaneously, along with axial tension, applied as a point load on a reference point located at the centre of one pipe end and fully coupled to the end face in all but the radial direction, as shown in Figure 4. At the opposite pipe end, a reference point is fully fixed in the centre and coupled to the end face.

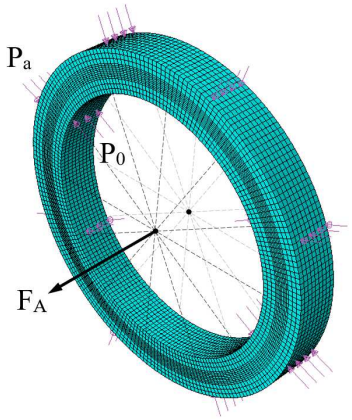

Figure 4. Axial point load and kinematic coupling

4.2. Validation of the Mechanical Model

The model was firstly validated for the case of combined pressure and tension prior to extending to include thermal load and defining temperature dependent properties on Abaqus. An analytical solution based on the Section 2 formulation excluding thermal component was developed in MATLAB for comparison with the FE model. Analysis was run for "A" and "B" TCP configurations with different laminate ply sequences (the basic $[\pm 55]_4$ and $[(\pm 15)_2/(90)_4]$ respectively) to validate fibre angle orientation under the following load conditions: P_0 = 40MPa; P_a = 20MPa; F_A = 50kN.

Through-thickness cylindrical stresses based on the MATLAB and FE models are shown in Figure 5. For both configurations MATLAB and Abaqus strongly agree. The Abaqus model was extended to thermomechanical by creating a coupled temperature-displacement step and employing appropriate thermal elements (C3D20RT). A suitable mesh was established by performing a refinement exercise.

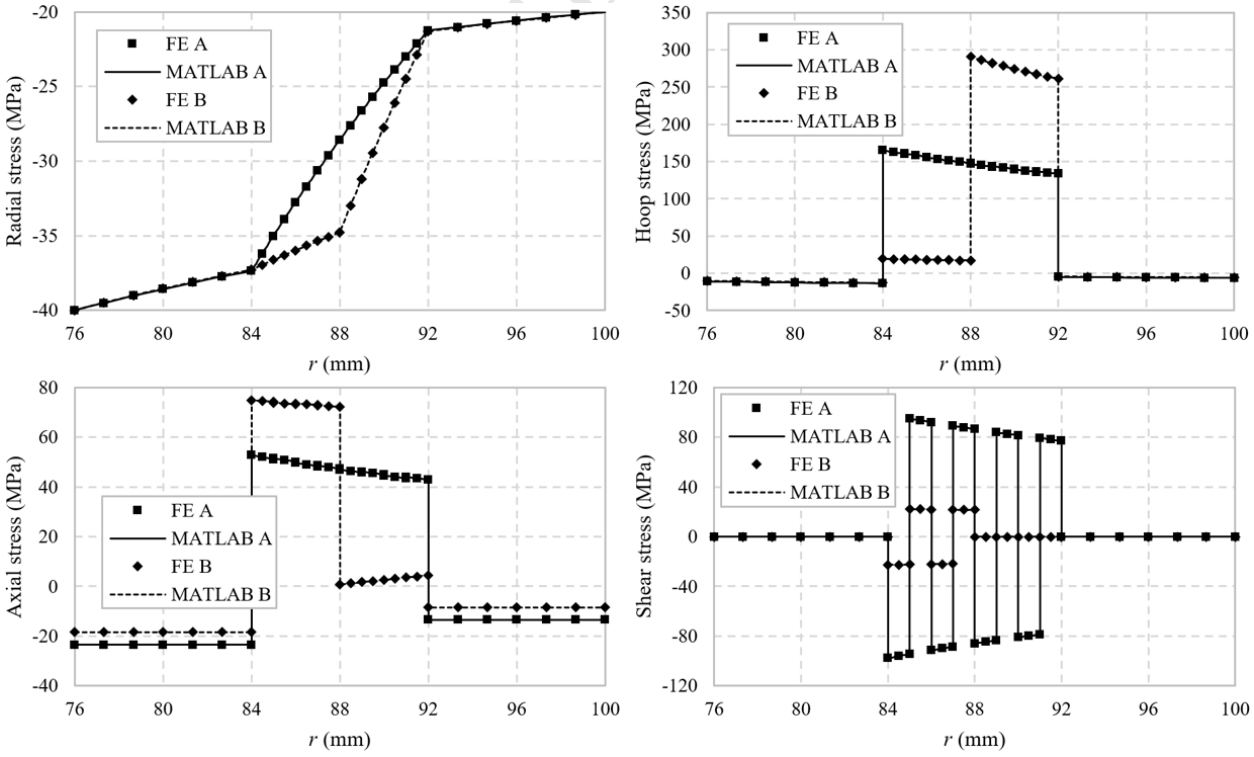

Figure 5. Validation of FE model stresses

4.3. Thermal Loading

During its service life, the internal temperature of a riser may vary considerably whereas the external seawater temperature will remain near constant in deepwater. In this study, increasing temperatures are applied as fixed boundary conditions on the internal surface. On the outer surface, a film coefficient is applied to simulate free convection to the surrounding environment.

5. Results and Discussion

Simulations were run for TCP under combined pressures, axial tension and thermal gradient illustrative of an SLHR operating in ultra deepwater (1,500m and beyond). In all cases internal pressure, external pressure and tension of 40MPa, 20MPa and 50kN respectively were applied (illustrative of operation at around 2,000m depth). Internal surface temperature was increased from 30 to 120°C to investigate the effects of increasing through-thickness gradient. The surrounding seawater temperature was 4°C with a heat transfer coefficient of $50 Wm^{-2}°C^{-1}$. An initial temperature of 23°C for the TCP was assumed.

5.1. Effects of Increasing Thermal Gradient

Through-thickness temperature distributions for the basic TCP (Table 1 configuration with $[\pm 55]_4$ laminate) under rising internal temperature are shown in Figure 6. Temperature decreases linearly from internal to external surfaces at different rates through the layers. The slope is steeper through the liners (r = 76 to 84mm, 92 to 100mm) than the laminate, owing to lower thermal conductivity and thus greater insulating characteristics. The temperature variation through the laminate increases with T_0. The outer surface temperature as a result of heat convection is 8.9 and 27.1°C for T_0 = 30 and 120°C respectively.

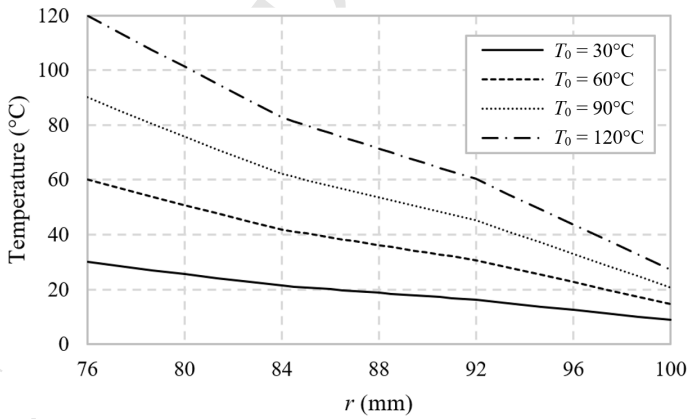

Figure 6. Temperature distributions for increasing T_0: basic TCP

Stress variations through the basic TCP under increasing T_0 are shown in Figure 7. Radial stress (σ_r) magnitude decreases linearly from the value of internal pressure on the inner surface to external pressure at the outer surface through the layers. Hoop (σ_θ), axial (σ_z) and shear ($\tau_{z\theta}$) stresses are predominantly carried by the laminate and increase with temperature gradient. The sign of the shear stress alternates with each ±55° ply.

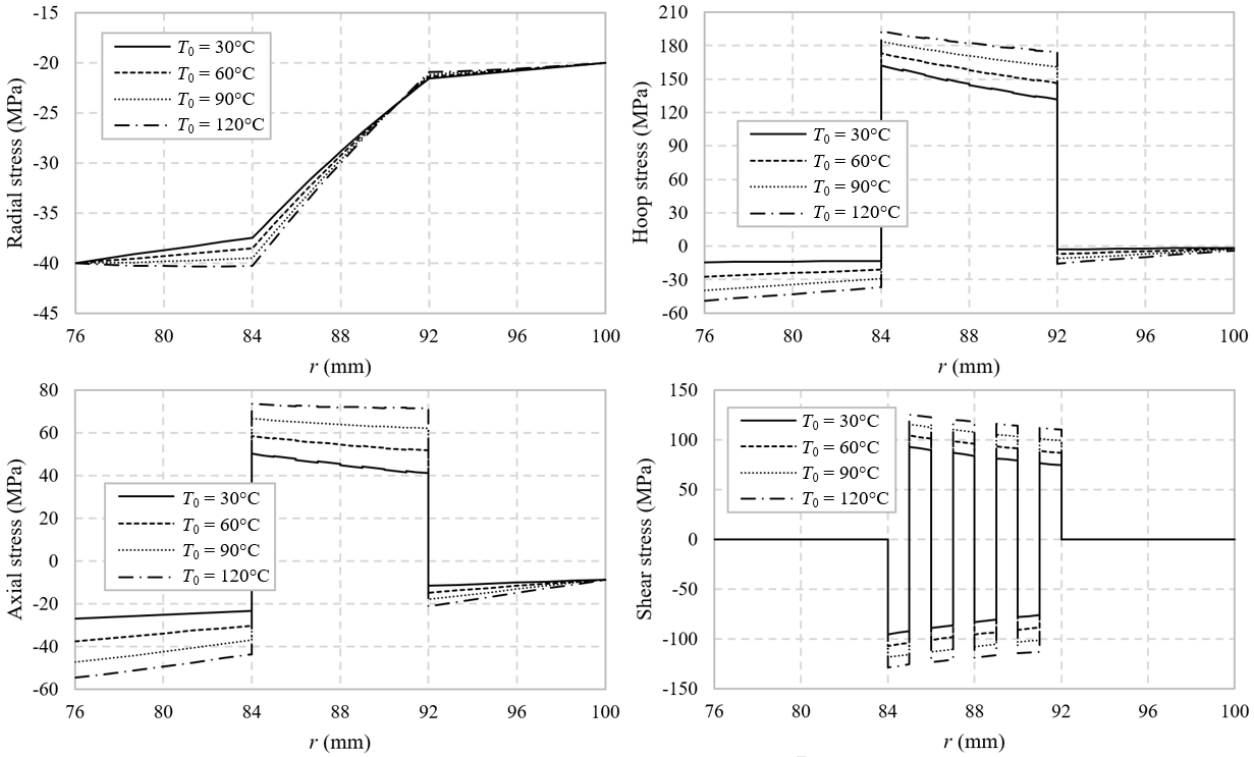

Figure 7. Stress variation in the basic TCP for increasing T_0

Von Mises failure coefficients through the liners are shown in Figure 8. The coefficient is generally smaller through the inner liner at increased T_0. In the outer liner, the coefficient decreases at r = 92mm with rising T_0 but is virtually unaltered at r_a. Failure coefficients through the laminate according to Max Stress and Tsai-Hill are shown in Figure 9. The Max Stress coefficient, governed by the compressive stress-to-strength ratio in the radial direction, increases slightly with T_0 at r = 84mm but is gradually less altered towards r = 92mm. This reflects the radial stress distributions in Figure 7, which are near identical for all T_0 towards r = 92mm. As per Max Stress, the interactive Tsai-Hill coefficient is also largest at r = 84mm for all cases. However, the increase with thermal gradient is uniform through the thickness, albeit marginal. The non-interactive simplistic nature of Max Stress is known to result in potential inaccuracies when predicting failure.

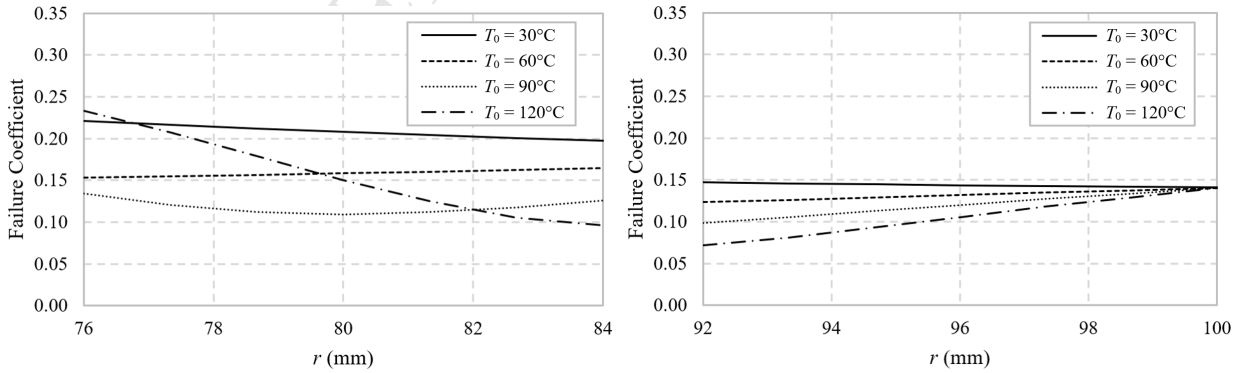

Figure 8. Von Mises coefficient through inner (left) and outer liner (right) for increasing T_0: basic TCP

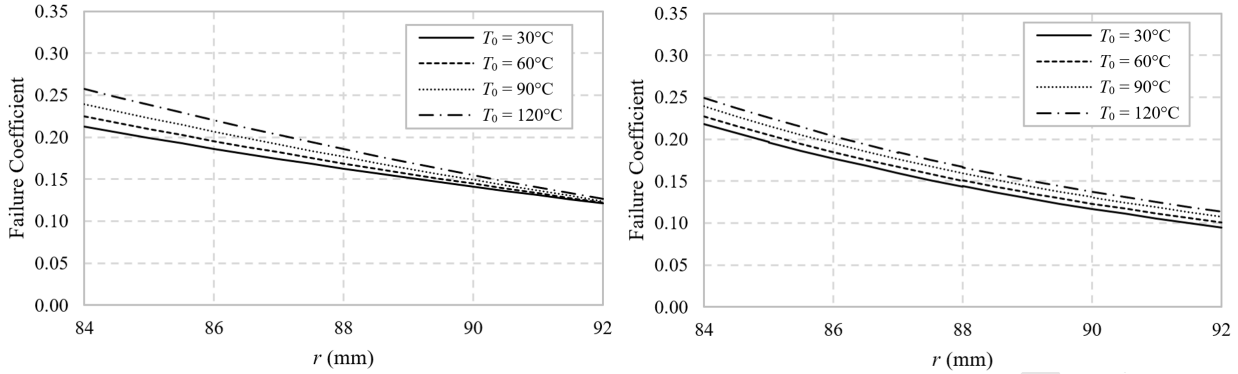

Figure 9. Through-laminate Max Stress (left) and Tsai-Hill coefficient (right) for increasing T_0: basic TCP

5.2. Effects of Varying Liner Thickness

Here, we investigate the effects of varying the thickness of the liners concurrently with respect to the laminate, the dimensions of which are kept constant. Temperature distributions for 4mm thick liner (4:8:4) and 12mm thick liner (12:8:12) configurations are shown in Figure 10. At higher gradients, the laminate temperature is hotter with thin liners and the difference through the laminate thickness is greater. The drop in temperature through the 4:8:4 laminate is almost double that of the 12:8:12, dropping from 94.2 to 62.5°C compared to 75.9 to 58.5°C. Thicker liners effectively regulate the temperature variation through the central laminate.

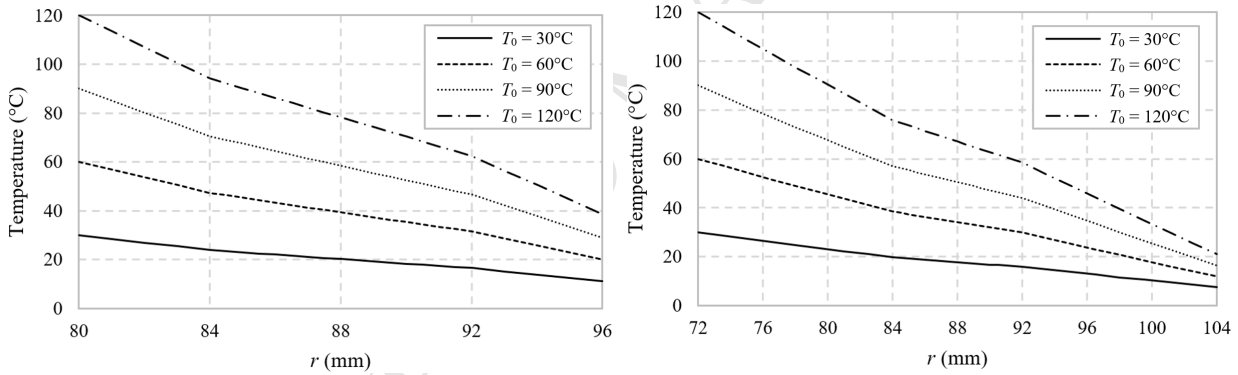

Figure 10. Temperature distributions for increasing T_0: 4:8:4 (left) and 12:8:12 (right)

Von Mises coefficients through 4mm and 12mm liners are shown in Figure 11. The coefficient increases significantly in the 4mm inner liner at the highest T_0 but varies only slightly in the 4mm outer liner with T_0. On the other hand, the coefficient is smaller for the inner 12mm liner at higher thermal gradients and becomes highly nonlinear at T_0 = 120°C. The coefficient decreases in the outer 12mm liner with rising thermal gradient but for a small increase towards r_a. At higher thermal gradients, thicker liners are superior in terms of affording higher practical safety factor, particularly in the inner liner. As can be seen in Figure 10, the differences in temperature between load cases are greatest in the inner liner, which result in more drastic variation of the failure coefficient with increasing T_0.

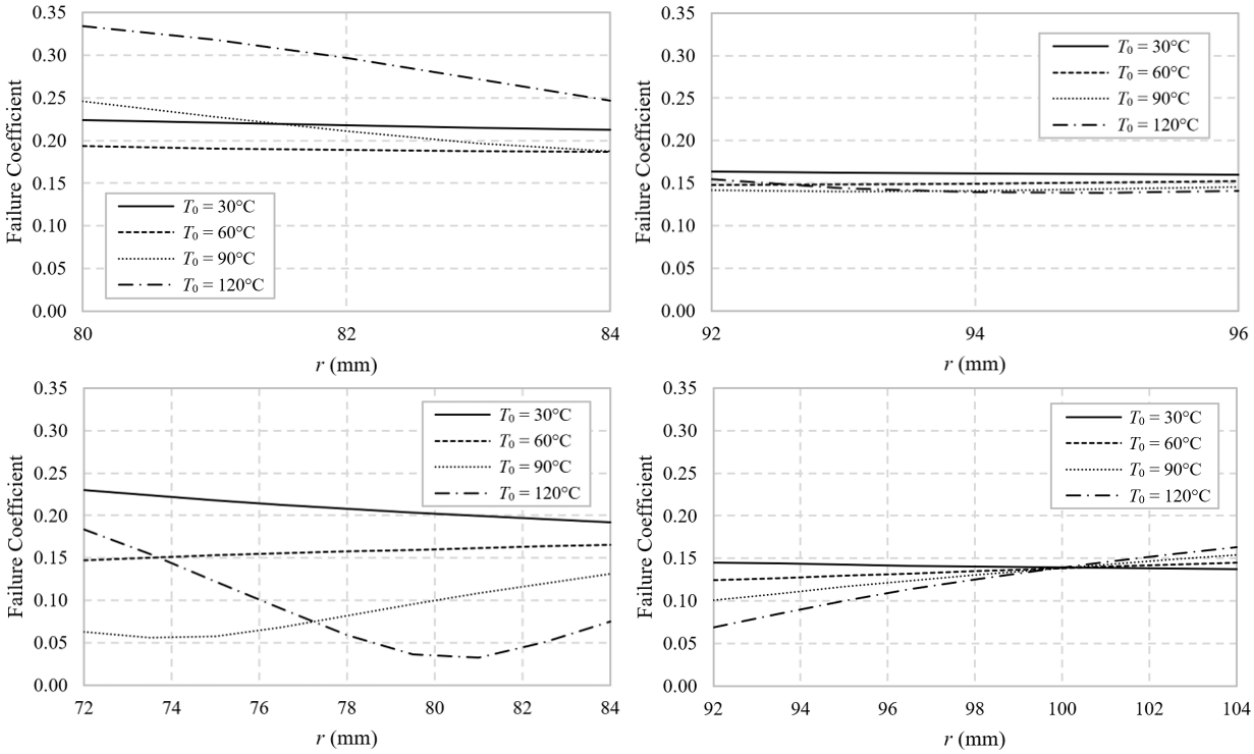

Figure 11. Von Mises coefficient through inner (left) and outer liner (right) for increasing T_0: 4:8:4 (top) and 12:8:12 (bottom)

4:8:4 and 12:8:12 through-laminate Max Stress and Tsai-Hill distributions are shown in Figures 12 and 13. The Max Stress coefficient decreases bilinearly through the 4:8:4 laminate, as the governing failure mode switches from radial compression in the innermost plies to in-plane shear in the outermost. In the case of 12mm liners, the coefficient is governed entirely by radial compression and with rising T_0 the largest increase is observed at r = 84mm, as we have earlier seen. The Tsai-Hill coefficient decreases slightly with rising T_0 through the 4:8:4 laminate. Conversely, the coefficient increases significantly for the 12:8:12 configuration. For the 12mm liner configuration, the Max Stress criterion significantly under-predicts failure compared to Tsai-Hill.

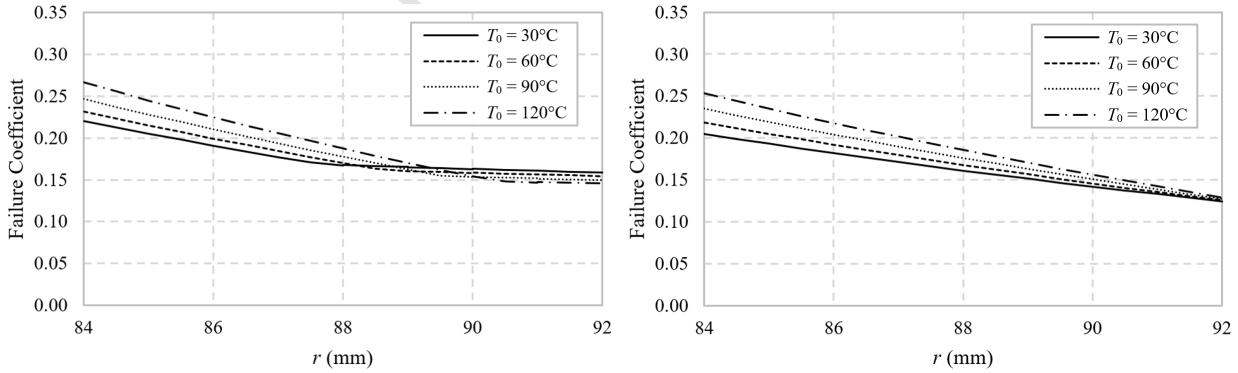

Figure 12. Through-laminate Max Stress coefficient for increasing T_0: 4:8:4 (left) and 12:8:12 (right)

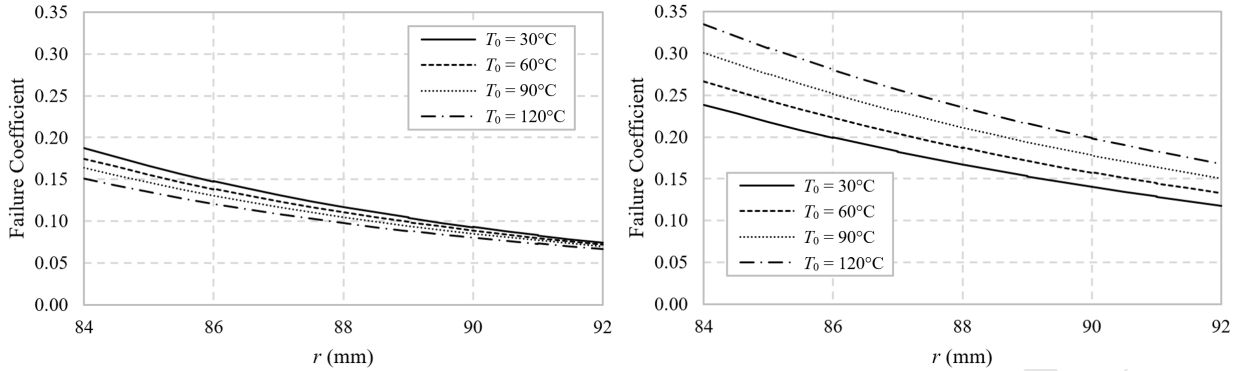

Figure 13. Through-laminate Tsai-Hill coefficient for increasing T_0: 4:8:4 (left) and 12:8:12 (right)

In summary, for the TCP considered here, von Mises failure coefficient in a thin inner liner increases with rising thermal gradient but laminate failure is not significantly altered, whereas thick liners are less prone to failure at higher gradients but the Tsai-Hill coefficient increases uniformly and substantially through the laminate with thick liners. Recalling that the liner primary function is to provide fluid tightness and wear resistance, the implications of using thin liners must be assessed e.g. for cracking.

5.3. Comparison of Thick Inner or Outer Liner

In this section, we investigate the failure response of a configuration with thin inner and thick outer liner, and vice versa, as opposed to liners of equal thickness. Von Mises coefficients through 4:8:12 and 12:8:4 configuration liners are shown in Figure 14. The coefficient is largest through the thick inner liner at T_0 = 30°C. For the thin inner liner, the coefficient is largest at r_0 for the T_0 = 120°C case. In both cases the outer liner coefficient is largest for the smallest T_0. The coefficient exhibits nonlinear behaviour in both thick liners at high thermal gradient. As before, the effects of rising gradient are greatest in the inner liner, regardless of whether a thin inner and thick outer liner or vice versa is used.

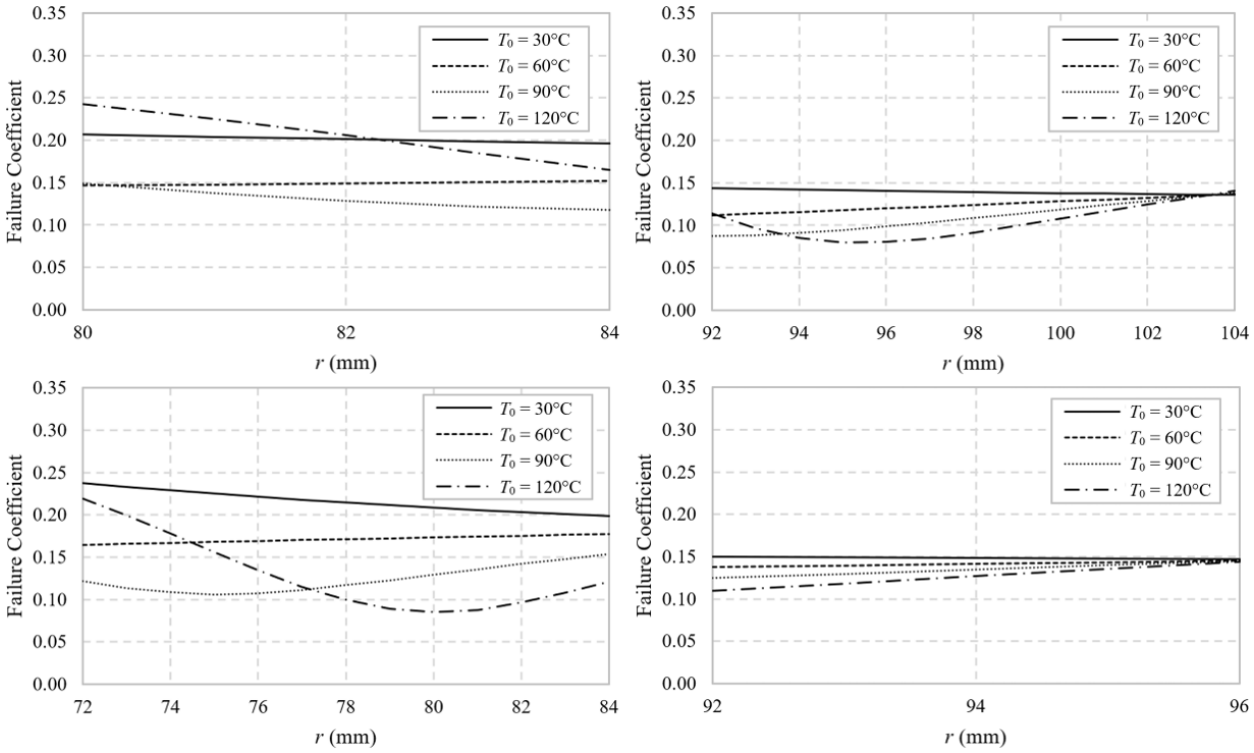

Figure 14. Von Mises coefficient through inner (left) and outer liner (right) for increasing T_0: 4:8:12 (top) and 12:8:4 (bottom)

Tsai-Hill coefficients through the 4:8:12 and 12:8:4 laminates are shown in Figure 15. At T_0 = 30°C the coefficients for both cases are near identical. The coefficient increases greatly with rising T_0 for the 12:8:4 configuration but remains virtually unchanged for the 4:8:12 case. From a practical point-of-view, for the same overall TCP thickness a thin inner and thick outer liner (4:8:12) is superior to the opposite configuration in terms of lower predicted Tsai-Hill laminate failure and only slightly greater liner von Mises coefficient at high thermal gradient.

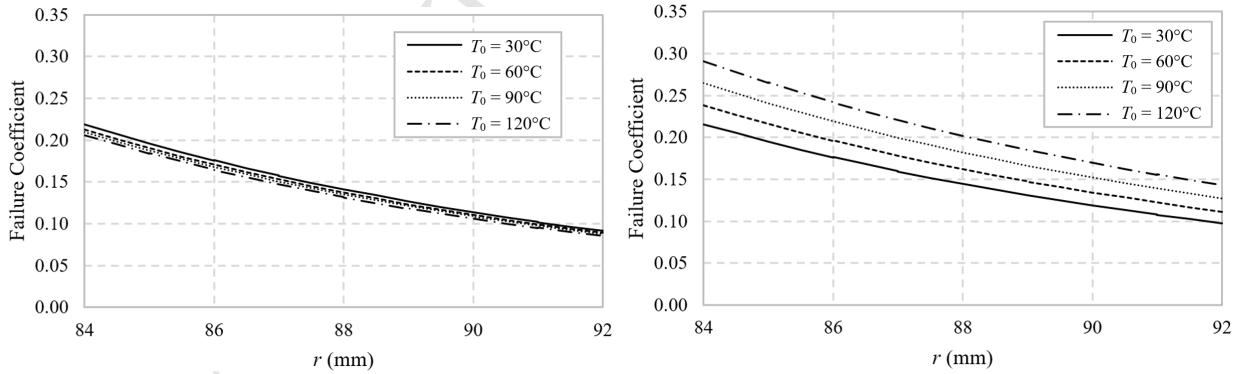

Figure 15. Through-laminate Tsai-Hill coefficient for increasing T_0: 4:8:12 (left) and 12:8:4 (right)

5.4. Discussion

In the scenarios investigated, the laminate Tsai-Hill coefficient was lowest for the TCP with thin (4mm) liners. However, large liner failure coefficient was observed, particularly in the inner liner at high thermal gradient. As opposed to utilising two thick (12mm) liners, which are less prone to failure but cause a substantial rise in laminate Tsai-Hill coefficient, an optimal design can be achieved by utilising a thin

inner and thick outer liner. In this case, laminate Tsai-Hill coefficient is lower and more stable at temperature, and the liner von Mises coefficient is only marginally higher than the opposite configuration with the same overall thickness. A thick outer liner also offers enhanced resistance to external wear and tear. However, the designer should consider the implications of a larger outer radius, e.g. in terms of bend radius (for spooling) and external fluid mechanics. The local material failure model presented can be used in conjunction with global riser analysis tools for global-local analysis.

This study has highlighted the importance of considering varying internal operating temperature for the practical application of TCP risers. High internal-to-external thermal gradient may lead to highly nonlinear effects in failure coefficients through thick liners, particularly a thick inner liner. The inner liner will experience larger changes in temperature during deepwater operation than the outer liner and the effects of rising internal temperature on failure coefficient are greater regardless of whether the inner liner is thinner or thicker than the outer. Appropriate optimisation of liner thickness can regulate the extent to which the laminate failure coefficient changes with varying internal operating temperature.

6. Conclusions

In this paper, a 3D FE model was developed to analyse stress state in TCP under combined pressure, tension and thermal gradient considering temperature-dependent material properties. From obtained stresses, through-thickness failure coefficient was analysed according to von Mises through isotropic liners and Max Stress and Tsai-Hill criteria through the laminate for illustrative SLHR load cases. The internal surface temperature was increased to investigate rising internal-to-external thermal gradient.

The effects of varying the liner thickness with respect to the central laminate were examined. In practical terms, varying the liner thickness creates a trade-off between liner and laminate safety factor as the thermal gradient is increased. Tsai-Hill coefficient through a laminate with equally thin liners does not change significantly with thermal gradient, however the von Mises failure coefficient in the inner liner increases considerably. On the other hand, equally thick liners are not more prone to yielding at increased thermal gradients but interactive failure coefficient of the central laminate increases.

For the TCP considered here, a thin inner and thick outer liner is superior to the opposite configuration in terms of lower laminate Tsai-Hill failure coefficient. Whilst this configuration appears optimal for the studied operating conditions, the designer should consider the implications, e.g. in terms of through-liner cracking, external fluid mechanics and bending of the pipe during transportation and installation. Global riser analysis tools can be used to determine the inputs for the TCP failure model presented here, i.e. to perform global-local analysis.

Acknowledgements

The authors wish to thank Dr Oleksandr Menshykov and Dr Maryna Menshykova of the Centre for Micro- and Nanomechanics, University of Aberdeen, for providing MATLAB script for validation purposes.

References

[1] Guz, I.A., Menshykova, M., Paik, J.K., 2017. Thick-walled composite tubes for offshore applications: an example of stress and failure analysis for filament-wound multi-layered pipes. Ships and Offshore Structures 12 (3), 304-322.

[2] Menshykova, M., Guz, I.A., 2014. Stress analysis of layered thick-walled composite pipes subjected to bending loading. International Journal of Mechanical Sciences 88, 289-299.

[3] Bai, Y., Wang, N., Cheng, P., Qiao, H., Yu, B., 2015. Collapse and buckling behaviors of reinforced thermoplastic pipe under external pressure. Journal of Offshore Mechanics and Arctic Engineering 137 (4), 041401.

[4] Kruijer, M.P., Warnet, L.L., Akkerman, R., 2005. Analysis of the mechanical properties of a reinforced thermoplastic pipe (RTP). Composites Part A: Applied Science and Manufacturing 36 (2), 291-300.

[5] Ashraf, M.A., Morozov, E.V., Shankar, K., 2014. Flexure analysis of spoolable reinforced thermoplastic pipes for offshore oil and gas applications. Journal of Reinforced Plastics and Composites 33 (6), 533-542.

[6] Yu, K., Morozov, E.V., Ashraf, M.A., Shankar, K., 2015. Analysis of flexural behaviour of reinforced thermoplastic pipes considering material nonlinearity. Composite Structures 119, 385-393.

[7] Yu, K., Morozov, E.V., Ashraf, M.A., Shankar, K., 2015. Numerical analysis of the mechanical behaviour of reinforced thermoplastic pipes under combined external pressure and bending. Composite Structures 131, 453-461.

[8] Bai, Y., Xu, W., Cheng, P., Wang, N., Ruan, W., 2014. Behaviour of reinforced thermoplastic pipe (RTP) under combined external pressure and tension. Ships and Offshore Structures 9 (4), 464-474.

[9] Bai, Y., Ruan, W., Cheng, P., Yu, B., Xu, W., 2014. Buckling of reinforced thermoplastic pipe (RTP) under combined bending and tension. Ships and Offshore Structures 9 (5), 525-539.

[10] Li, G.H., Wang, W.J., Jing, Z.J., Ma, X.C., Zuo, L.B., 2016. Experimental Study and Finite Element Analysis of Critical Stresses of Reinforced Thermoplastic Pipes Under Various Loads. Strength of Materials 48 (1), 165-172.

[11] Kruijer, M.P., Warnet, L.L., Akkerman, R., 2006. Modelling of the viscoelastic behaviour of steel reinforced thermoplastic pipes. Composites Part A: Applied Science and Manufacturing 37 (2), 356-367.

[12] Xia, M., Kemmochi, K., Takayanagi, H., 2001. Analysis of filament-wound fiber-reinforced sandwich pipe under combined internal pressure and thermomechanical loading. Composite Structures 51 (3), 273-283.

[13] Akçay, İ.H., Kaynak, İ., 2005. Analysis of multilayered composite cylinders under thermal loading. Journal of Reinforced Plastics and Composites 24 (11), 1169-1179.

[14] Bakaiyan, H., Hosseini, H., Ameri, E., 2009. Analysis of multi-layered filament-wound composite pipes under combined internal pressure and thermomechanical loading with thermal variations. Composite Structures 88 (4), 532-541.

[15] Zhang, Q., Wang, Z.W., Tang, C.Y., Hu, D.P., Liu, P.Q., Xia, L.Z., 2012. Analytical solution of the thermo-mechanical stresses in a multilayered composite pressure vessel considering the influence of the closed ends. International Journal of Pressure Vessels and Piping 98, 102-110.

[16] Wang, L., Zheng, C., Wei, S., Wei, Z., 2016. Micromechanics-based progressive failure analysis of carbon fiber/epoxy composite vessel under combined internal pressure and thermomechanical loading. Composites Part B: Engineering 89, 77-84.

[17] Vedeld, K., Sollund, H.A., 2014. Stresses in heated pressurized multi-layer cylinders in generalized plane strain conditions. International Journal of Pressure Vessels and Piping, 120-121, 27-35.

[18] Sollund, H.A., Vedeld, K., Hellesland, J., 2014. Efficient analytical solutions for heated and pressurized multi-layer cylinders. Ocean Engineering, 92, 285-295.

[19] Yeo, W.H., Purbolaksono, J., Aliabadi, M.H., Ramesh, S., Liew, H.L., 2017. Exact solution for stresses/displacements in a multilayered hollow cylinder under thermo-mechanical loading. International Journal of Pressure Vessels and Piping 151, 45-53.

[20] Xia, M., Takayanagi, H., Kemmochi, K., 2001. Analysis of multi-layered filament-wound composite pipes under internal pressure. Composite Structures 53 (4), 483-491.

[21] Herakovich, C.T., 1998. Mechanics of fibrous composites. New York (NY): Wiley.

[22] Haji-Sheikh, A., Beck, J.V., Agonafer, D., 2003. Steady-state heat conduction in multi-layer bodies. International Journal of Heat and Mass Transfer 46 (13), 2363-2379.

[23] Cytec, 2012. APC-2 PEEK thermoplastic polymer technical data sheet.

[24] Coquill, S.L., Adams, D.F., 1989. Mechanical properties of several neat polymer matrix materials and unidirectional carbon fiber-reinforced composites. NASA CR-181805.

[25] Ramey, J. and Palazotto, A.,1989. A study of graphite/PEEK under high temperatures. G.M. Newaz, ed., Advances in Thermoplastic Matrix Composite Materials. Chelsea (MI): ASTM, 91-112.

[26] Yousefpour, A., Nejhad, M.N.G., 2004. Design, analysis, manufacture, and test of APC-2/AS4 thermoplastic composite pressure vessels for deep water marine applications. Journal of Composite Materials 38 (19), 1701-1732.

[27] Grove, S.M., 1988. Thermal modelling of tape laying with continuous carbon fibre-reinforced thermoplastic. Composites 19 (5), 367-375.

[28] Sun, C.T., Rui, Y., 1989. Orthotropic elasto-plastic behavior of AS4/APC-2 thermoplastic composite in compression. NASA CML 89-2.

[29] Rule, D.L., Sparks, L.L., 1989. Thermal conductivity of alumina fiber/epoxy and alumina fiber/PEEK from 4.2 to 310 K. Proceedings of the Twenty-First International Conference on Thermal Conductivity; October 15-18; Lexington, Kentucky.

[30] Jones, D.P., Leach, D.C., Moore, D.R., 1985. Mechanical properties of poly(ether-ether-ketone) for engineering applications. Polymer 26 (9), 1385-1393.

Appendix 1

The orthotropic stiffness matrix in material coordinates can be written in terms of engineering constants as:

$$[C] = \begin{bmatrix} C_{11} & C_{12} & C_{13} & 0 & 0 & 0 \\ C_{12} & C_{22} & C_{23} & 0 & 0 & 0 \\ C_{13} & C_{23} & C_{33} & 0 & 0 & 0 \\ 0 & 0 & 0 & C_{44} & 0 & 0 \\ 0 & 0 & 0 & 0 & C_{55} & 0 \\ 0 & 0 & 0 & 0 & 0 & C_{66} \end{bmatrix} = \begin{bmatrix} \frac{1}{E_1} & \frac{-\nu_{12}}{E_1} & \frac{-\nu_{13}}{E_1} & 0 & 0 & 0 \\ \frac{-\nu_{12}}{E_1} & \frac{1}{E_2} & \frac{-\nu_{23}}{E_2} & 0 & 0 & 0 \\ \frac{-\nu_{13}}{E_1} & \frac{-\nu_{23}}{E_2} & \frac{1}{E_3} & 0 & 0 & 0 \\ 0 & 0 & 0 & \frac{1}{G_{23}} & 0 & 0 \\ 0 & 0 & 0 & 0 & \frac{1}{G_{13}} & 0 \\ 0 & 0 & 0 & 0 & 0 & \frac{1}{G_{12}} \end{bmatrix}^{-1},$$

where subscripts 1, 2 and 3 refer to fibre longitudinal, transverse in-plane and out-of-plane directions respectively.

Layer off-axis stiffness constants are then transformed from constants along principal directions based on angle φ as follows [20]:

$$\{\bar{C}\}^{(k)} = [A]\{C\}^{(k)},$$

where:

$$\{\bar{C}\}^{(k)} = \left\{\bar{C}_{11}^{(k)}, \bar{C}_{12}^{(k)}, \bar{C}_{13}^{(k)}, \bar{C}_{16}^{(k)}, \bar{C}_{22}^{(k)}, \bar{C}_{23}^{(k)}, \bar{C}_{26}^{(k)}, \bar{C}_{33}^{(k)}, \bar{C}_{36}^{(k)}, \bar{C}_{44}^{(k)}, \bar{C}_{45}^{(k)}, \bar{C}_{55}^{(k)}, \bar{C}_{66}^{(k)}\right\}^T,$$

$$\{C\}^{(k)} = \left\{C_{11}^{(k)}, C_{22}^{(k)}, C_{33}^{(k)}, C_{12}^{(k)}, C_{13}^{(k)}, C_{23}^{(k)}, G_{23}^{(k)}, G_{12}^{(k)}, G_{13}^{(k)}\right\}^T.$$

The stiffness transformation matrix is:

$$[A]=\begin{bmatrix} m^4 & n^4 & 0 & 2m^2n^2 & 0 & 0 & 0 & 0 & 4m^2n^2 \\ m^2n^2 & m^2n^2 & 0 & m^4+n^4 & 0 & 0 & 0 & 0 & -4m^2n^2 \\ 0 & 0 & 0 & 0 & m^2 & n^2 & 0 & 0 & 0 \\ m^3n & -mn^3 & 0 & -m^3n+mn^3 & 0 & 0 & 0 & 0 & -2m^3n+2mn^3 \\ n^4 & m^4 & 0 & 2m^2n^2 & 0 & 0 & 0 & 0 & 4m^2n^2 \\ 0 & 0 & 0 & 0 & n^2 & m^2 & 0 & 0 & 0 \\ mn^3 & -m^3n & 0 & m^3n-mn^3 & 0 & 0 & 0 & 0 & 2m^3n-2mn^3 \\ 0 & 0 & 1 & 0 & 0 & 0 & 0 & 0 & 0 \\ 0 & 0 & 0 & 0 & mn & -mn & 0 & 0 & 0 \\ 0 & 0 & 0 & 0 & 0 & 0 & m^2 & n^2 & 0 \\ 0 & 0 & 0 & 0 & 0 & 0 & -mn & mn & 0 \\ 0 & 0 & 0 & 0 & 0 & 0 & n^2 & m^2 & 0 \\ m^2n^2 & m^2n^2 & 0 & -2m^2n^2 & 0 & 0 & 0 & 0 & (m^2-n^2)^2 \end{bmatrix},$$

where $m = \cos\varphi$ and $n = \sin\varphi$.

Similarly, the expansion coefficients in principal coordinates can be transformed to the cylindrical axis for the thermal strains [14]:

$$\begin{Bmatrix} \alpha_z \\ \alpha_\theta \\ \alpha_r \\ \alpha_{z\theta} \end{Bmatrix}^{(k)} = \begin{bmatrix} m^2 & n^2 & 0 \\ n^2 & m^2 & 0 \\ 0 & 0 & 1 \\ mn & -mn & 0 \end{bmatrix} \begin{Bmatrix} \alpha_1 \\ \alpha_2 \\ \alpha_3 \end{Bmatrix}^{(k)}.$$

Effects of Thermal Gradient on Failure of a Thermoplastic Composite Pipe (TCP) Riser Leg

James C. Hastie*, Igor A. Guz, Maria Kashtalyan
School of Engineering, University of Aberdeen, Scotland, UK
Centre for Micro- and Nanomechanics (CEMINACS)
**Corresponding author. Email: r03jh15@abdn.ac.uk*

Effects of Thermal Gradient on Failure of a Thermoplastic Composite Pipe (TCP) Riser Leg

Abstract

Thermoplastic composite pipe (TCP), consisting of a fibre-reinforced thermoplastic laminate fully bonded between homogeneous thermoplastic liners, is an ideal candidate to replace traditional steel riser pipes in deepwater where high specific strengths and moduli and corrosion resistance are advantageous. During operation, risers are subjected to combined mechanical and thermal loads. In the present paper, a 3D finite element (FE) model is developed to analyse stress state in a section of TCP under combined pressure, axial tension and thermal gradient, illustrative of a single-leg hybrid riser (SLHR) application. From the obtained stresses, through-thickness failure coefficient is evaluated based on appropriate failure criteria. The effects of increasing the internal-to-external thermal gradient are investigated considering temperature dependent material properties. The influence of varying the thickness of the isotropic liners with respect to the laminate is examined.

Keywords: Thermoplastic composite pipe; composite riser; thermal gradient

1. Introduction

Fibre-reinforced plastic (FRP) materials have been viewed as candidates to replace steels in deepwater exploration and production (E&P) applications for a number of advantages including high specific strengths and moduli and excellent corrosion resistance. Thermoplastic composite pipe (TCP) is an example of an FRP product attracting growing interest in the offshore E&P sector. TCP consists of a fibre-reinforced thermoplastic multi-ply laminate with inner and outer homogeneous thermoplastic liners, which provide fluid tightness and wear resistance. Figure 1 shows the basic construction. Polyethylene (PE), polyamide (PA) and polyetheretherketone (PEEK) thermoplastics are used, superior to thermosets in terms of ductility, toughness, impact resistance and stability at extreme temperatures. The thermoplastic is reinforced with tape- or filament-wound (FW) carbon, glass or aramid fibres to form the laminate. A melt-fusion process typified by leading manufacturers is used to fully bond all layers.

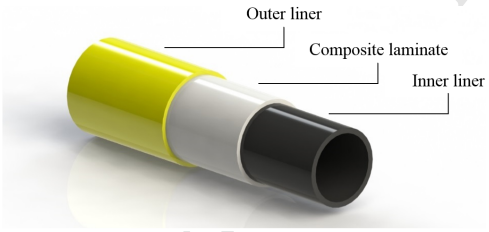

Figure 1. TCP configuration

The behaviour of multi-layered, fibre-reinforced pipes under mechanical loads for practical application has been studied for several decades (see reviews in [1,2]). The response of thermoplastic-based pipe of the tri-layer TCP construction specifically, often referred to in different sources as ‘reinforced thermoplastic pipe (RTP)’, under various discrete and combined mechanical loads relevant to subsea applications has also been studied in recent literature. Bai et al. [3] investigated external pressure

collapse of TCP consisting of aramid fibre and high-density polyethylene (HDPE) layers by theoretical, finite element (FE) and experimental methods. Kruijer et al. [4] investigated the behaviour of pressurised TCP considering slack of non-impregnated aramid reinforcement cords. Ashraf et al. [5] used FE modelling to investigate bending-induced buckling of carbon/PEEK TCP. Bending of aramid/PE TCP was investigated numerically by Yu et al. [6], accounting for strain-dependent nonlinearity. The behaviour of TCP under combined pressure and bending [7], pressure-tension [8] and bending-tension [9] has been studied largely by numerical means. Variations of TCP have been developed and studied, including multi-layered plastic pipes reinforced with steel wires or strips as an alternative to, or in conjunction with, non-metallic fibres [10,11]. Weight added by steel can improve stability for certain subsea piping systems.

In addition to mechanical loads, subsea tubulars are subjected to uniform temperature change (e.g. deploying into cool seawater) and thermal gradients during operation (i.e. resulting from the mismatch between hot internal fluids and external seawater). Literature pertaining to FRP and multi-layered pipes under thermomechanical load is less widely available. Xia et al. [12] presented an elastic solution based on classical lamination theory for pressurised sandwich pipes with isotropic core and orthotropic skins subjected to temperature change. Akçay and Kaynak [13] used analytical expressions to investigate failure of multi-layered FRP cylinders under pressure and uniform thermal load for plane-strain and closed-end conditions. A 3D elasticity solution for multi-layered FW pipes subjected to internal pressure and temperature gradient was presented by Bakaiyan et al. [14]. A closed-form stress solution for pressurised vessels with multiple isotropic layers subjected to thermal load was presented by Zhang et al. [15]. Wang et al. [16] proposed a strategy for predicting failure of a carbon/epoxy vessel under pressure and thermal loading based on material property degradation and micromechanics of failure (MMF) criterion. Analytical solutions for stresses and displacements in heated and pressurised multi-layered pipes were developed by Vedeld and Sollund [17] and Sollund et al. [18]. The solution of Vedeld and Sollund [17], which assumed uniform temperature distribution within each layer, was subsequently refined by Yeo et al. [19], who found their refined solution to produce more accurate predictions than the original.

In general, literature on thermal loading of composite pipes has largely been limited to analytical studies. A numerical model, developed for example in dedicated FE software packages such as Abaqus or ANSYS, would allow a wide array of mechanical and thermal load combinations to be studied. Furthermore, defects such as delamination can be introduced where this may prove analytically complex or unfeasible.

Revision 28/1/2019 21:51
Deleted: on

Revision 28/1/2019 21:51
Deleted: packages

As well as a requirement for greater overall understanding of the behaviour of composite pipes such as TCP under thermal load, there is a particular need for investigating behaviour when accounting for the temperature dependence of material properties. Composite properties are most often taken to be constant in existing literature, likely a by-product of the lack of available data to fully define a material over an appropriate temperature range. To more accurately predict stress and strain states and resulting failure it is crucial that temperature dependence is accounted for.

In the present paper, the problem of TCP under combined pressure, axial tension and thermal gradient illustrative of a deepwater riser application is considered. A 3D FE model is developed for predicting stress state under the combined loading taking into account temperature dependent carbon/PEEK material properties uniquely compiled and extrapolated from literature. From obtained stress distributions, through-thickness failure coefficients according to von Mises criterion for isotropic liners and Maximum Stress and Tsai-Hill criteria for orthotropic laminate are analysed. The effects of increasing the internal-to-external thermal gradient on failure are investigated. The influence of varying liner thickness with respect to the central laminate is also examined.

2. Problem Formulation

A single-leg hybrid riser (SLHR) system, illustrated in Figure 2, is an application in which the benefits of TCP can be exploited to great economic effect. The riser leg, tensioned by buoyancy to avoid buckling, is isolated from vessel motions by a flexible jumper. Let us consider a section along the leg. During operation, the section is subjected to internal and external pressures (P_0 and P_a), axial tension (F_A), and internal and external surfaces temperatures (T_0 and T_a).

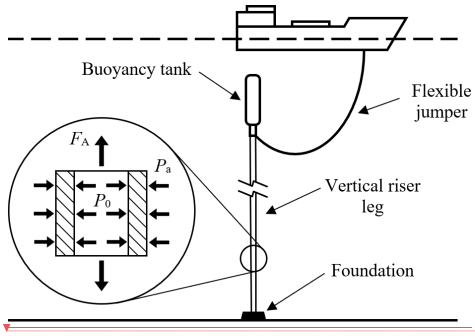

Figure 2. SLHR system

Here, we consider the section to be TCP with N layers as illustrated in Figure 3. Layers $k = 1$ and $k = N$ are isotropic liners and the remaining layers are orthotropic plies that together form the laminate. Under axisymmetric loading, stresses and strains are independent of the hoop coordinate, θ. Axial (z) and radial (r) displacements depend only on the corresponding directions i.e. [20]:

$$u_z = u_z(z), \quad u_\theta = u_\theta(r,z), \quad u_r = u_r(r), \tag{1}$$

where u_i denotes displacement in z, θ and r.

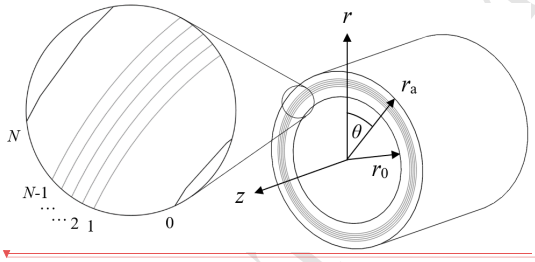

Figure 3. TCP in cylindrical coordinates

The strain-displacement relations are written as [20,21]:

$$\varepsilon_z^{(k)} = \frac{du_z^{(k)}}{dz} = \varepsilon_0, \quad \varepsilon_\theta^{(k)} = \frac{u_r^{(k)}}{r}, \quad \varepsilon_r^{(k)} = \frac{du_r^{(k)}}{dr},$$

Revision 28/1/2019 21:51
Formatted: Font:Not Italic

Revision 28/1/2019 21:51
Formatted: Font:Not Italic

Revision 28/1/2019 21:51
Formatted: Font:Not Italic

Revision 28/1/2019 21:51
Formatted: Font:Not Italic

Revision 28/1/2019 21:51
Formatted: Font:Not Italic

Revision 28/1/2019 21:51
Formatted: Centered

Revision 28/1/2019 21:51

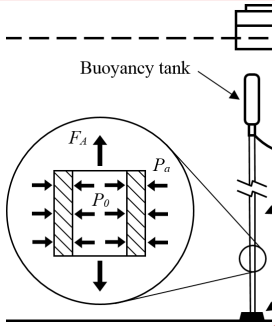

Deleted:

Revision 28/1/2019 21:51

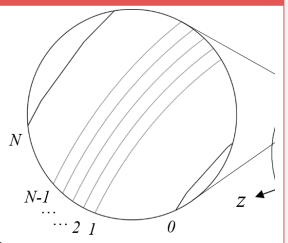

Deleted:

Revision 28/1/2019 21:51
Deleted: $\varepsilon_\theta^{(k)} = \frac{u_r^{(k)}}{r}, \quad \varepsilon_z^{(k)} = \frac{du_z^{(k)}}{dz} = \varepsilon_0,$.

$$\gamma_{\theta r}^{(k)} = \frac{du_\theta^{(k)}}{dr} - \frac{u_\theta^{(k)}}{r}, \quad \gamma_{zr}^{(k)} = 0, \quad \gamma_{z\theta}^{(k)} = \frac{du_\theta^{(k)}}{dz} = \gamma_0 r, \tag{2}$$

where γ_0 is a pipe twist per unit length and ε_0 is constant.

Layer stresses and strains in cylindrical coordinates are related by the constitutive equations [21]:

$$\begin{Bmatrix} \sigma_z \\ \sigma_\theta \\ \sigma_r \\ \tau_{\theta r} \\ \tau_{zr} \\ \tau_{z\theta} \end{Bmatrix}^{(k)} = \begin{bmatrix} \bar{C}_{11} & \bar{C}_{12} & \bar{C}_{13} & 0 & 0 & \bar{C}_{16} \\ \bar{C}_{12} & \bar{C}_{22} & \bar{C}_{23} & 0 & 0 & \bar{C}_{26} \\ \bar{C}_{13} & \bar{C}_{23} & \bar{C}_{33} & 0 & 0 & \bar{C}_{36} \\ 0 & 0 & 0 & \bar{C}_{44} & \bar{C}_{45} & 0 \\ 0 & 0 & 0 & \bar{C}_{45} & \bar{C}_{55} & 0 \\ \bar{C}_{16} & \bar{C}_{26} & \bar{C}_{36} & 0 & 0 & \bar{C}_{66} \end{bmatrix}^{(k)} \begin{Bmatrix} \varepsilon_z - \alpha_z \Delta T \\ \varepsilon_\theta - \alpha_\theta \Delta T \\ \varepsilon_r - \alpha_r \Delta T \\ \gamma_{\theta r} \\ \gamma_{zr} \\ \gamma_{z\theta} - 2\alpha_{z\theta} \Delta T \end{Bmatrix}^{(k)}, \tag{3}$$

where $\bar{C}_{ij}$ are the transformed stiffness constants corresponding to a fibre-reinforced layer orientated at angle φ, which describes the offset of the fibre longitudinal from the cylindrical z direction; α_z, α_θ, α_r and $\alpha_{z\theta}$ are the cylindrical coefficients of thermal expansion; ΔT is the change in temperature. The transformation of stiffness constants from material coordinates to off-axis directions is demonstrated in Appendix 1. Note that whilst the plies are orthotropic, the behaviour is strictly monotropic in relation to the global axis (i.e. fibre direction not aligned with z).

Under axisymmetric internal-to-external temperature differential, ΔT depends on the radial temperature distribution, $T(r)$:

$$\Delta T = T(r) - T_{\text{ref}}, \tag{4}$$

where T_{ref} is the initial (or reference) temperature.

The equation for steady-state heat conduction considering no heat generation for a multi-layered pipe in cylindrical coordinates is expressed as [14,15]:

$$\frac{\partial^2 T(r)}{\partial r^2} + \frac{1}{r}\frac{\partial T(r)}{\partial r} = 0. \tag{5}$$

Heat flux must satisfy continuity for layers $k = 1, 2, \ldots, N\text{-}1$:

$$q^{(k)}(r_k) = q^{(k+1)}(r_k), \tag{6}$$

where the heat flux through layer k with radial thermal conductivity λ_r (orthotropic λ_3) is obtained using Fourier's law:

$$q^{(k)} = -\lambda_r^{(k)} \frac{\partial T^{(k)}}{\partial r}. \tag{7}$$

Combining Equations (5) and (6) it can be shown that [15,22]:

Revision 28/1/2019 21:51
Deleted: $\gamma_{zr}^{(k)} = 0,$

Revision 28/1/2019 21:51
Formatted: Font:Not Italic

Revision 28/1/2019 21:51
Formatted: Font:Not Italic

Revision 28/1/2019 21:51
Deleted: Stresses and strains are related by the iso- or orthotropic stiffness matrices [21]. Here, we shall demonstrate the less trivial orthotropic relations.

Revision 28/1/2019 21:51
Formatted: Indent: First line: 0 cm

Revision 28/1/2019 21:51
Deleted: $\begin{Bmatrix} \sigma_z \\ \sigma_\theta \\ \sigma_r \\ \tau_{\theta r} \\ \tau_{zr} \\ \tau_{z\theta} \end{Bmatrix}^{(ortho)} = \begin{bmatrix} \bar{C}_{11} & \bar{C}_{12} & \bar{C}_{13} & 0 & 0 & \bar{C}_{16} \\ \bar{C}_{12} & \bar{C}_{22} & \bar{C}_{23} & 0 & 0 & \bar{C}_{26} \\ \bar{C}_{13} & \bar{C}_{23} & \bar{C}_{33} & 0 & 0 & \bar{C}_{36} \\ 0 & 0 & 0 & \bar{C}_{44} & \bar{C}_{45} & 0 \\ 0 & 0 & 0 & \bar{C}_{45} & \bar{C}_{55} & 0 \\ \bar{C}_{16} & \bar{C}_{26} & \bar{C}_{36} & 0 & 0 & \bar{C}_{66} \end{bmatrix}^{(ortho)} \begin{Bmatrix} \varepsilon_z \\ \varepsilon_\theta \\ \varepsilon_r \\ \\ \\ \gamma_{z\theta} \end{Bmatrix}$

Revision 28/1/2019 21:51
Deleted: α_i

Revision 28/1/2019 21:51
Deleted: α_{ij}

Revision 28/1/2019 21:51
Deleted: T_{ref}

Revision 28/1/2019 21:51
Formatted: Font:Not Italic

Revision 28/1/2019 21:51
Formatted: Font:Not Italic

Revision 28/1/2019 21:51
Deleted: [15]:

$$\frac{T^{(k-1)}-T^{(k)}}{T^{(k)}-T^{(k+1)}}=\frac{\lambda_r^{(k+1)}}{\lambda_r^{(k)}}\frac{\ln\left(\frac{r^{(k)}}{r^{(k-1)}}\right)}{\ln\left(\frac{r^{(k+1)}}{r^{(k)}}\right)}. \quad (8)$$

The temperature at the interface between the *k*th and *k*+1th layer is deduced as [15]:

$$T^{(k)}=\frac{\lambda_r^{(k)}T^{(k-1)}\ln\left(\frac{r^{(k+1)}}{r^{(k)}}\right)+\lambda_r^{(k+1)}T^{(k+1)}\ln\left(\frac{r^{(k)}}{r^{(k-1)}}\right)}{\lambda_r^{(k)}\ln\left(\frac{r^{(k+1)}}{r^{(k)}}\right)+\lambda_r^{(k+1)}\ln\left(\frac{r^{(k)}}{r^{(k-1)}}\right)}. \quad (9)$$

Thus, the temperature at radius r in an arbitrary layer k is [15]:

$$T(r)=\frac{T^{(k)}-T^{(k-1)}}{\ln\left(\frac{r^{(k)}}{r^{(k-1)}}\right)}\ln\frac{r}{r^{(k)}}+T^{(k)}. \quad (10)$$

The distribution under uniform internal and external temperature is bound by:

$$T(r_0)=T_0, \qquad T(r_a)=T_a, \quad (11)$$

where r_0 and r_a are the inner and outer radius respectively.

The equilibrium equations for a long axisymmetric tube under prescribed loading are [20,21]:

$$\frac{d\sigma_r^{(k)}}{dr}+\frac{\sigma_r^{(k)}-\sigma_\theta^{(k)}}{r}=0, \quad (12a)$$

$$\frac{d\tau_{\theta r}^{(k)}}{dr}+\frac{2\tau_{\theta r}^{(k)}}{r}=0, \quad (12b)$$

$$\frac{d\tau_{zr}^{(k)}}{dr}+\frac{\tau_{zr}^{(k)}}{r}=0. \quad (12c)$$

From (12b) and (12c) we obtain:

$$\tau_{\theta r}^{(k)}=\frac{A^{(k)}}{r^2}, \qquad \tau_{zr}^{(k)}=\frac{B^{(k)}}{r}, \quad (13)$$

where $A^{(k)}$ and $B^{(k)}$ are unknown integration constants.

Revision 28/1/2019 21:51
Deleted: 8)

Revision 28/1/2019 21:51
Formatted: Tabs:Not at 8.25 cm + 16.5 cm

Revision 28/1/2019 21:51
Deleted: 9

Revision 28/1/2019 21:51
Deleted: $(r_a) = T_a,$ (10

Revision 28/1/2019 21:51
Formatted ... [1]

Revision 28/1/2019 21:51
Moved down [1]: The orthotropic stiffness matrix in material coordinates can be written in terms of engineering constants as: ... [2]

Revision 28/1/2019 21:51
Formatted: Indent: First line: 0 cm

Revision 28/1/2019 21:51
Deleted: (11) ... [3]

Revision 28/1/2019 21:51
Moved down [2]: where subscripts ... [4]

Revision 28/1/2019 21:51
Formatted ... [5]

Revision 28/1/2019 21:51
Deleted: We note that $E_2 = E_3$, $\nu_{12} =$ ... [6]

Revision 28/1/2019 21:51
Moved down [3]: based on angle φ ... [7]

Revision 28/1/2019 21:51
Deleted: $\{\bar{C}_{ij}^{(k)}\} = [A_{kl}]\{C_{ij}^{(k)}\},$ (12a) ... [8]

Revision 28/1/2019 21:51
Moved down [4]: where:

Revision 28/1/2019 21:51
Moved down [5]: , ... [9]

Revision 28/1/2019 21:51
Deleted: $\{C_{ij}^{(k)}\} =$ ... [10]

Revision 28/1/2019 21:51
Moved down [6]:

Revision 28/1/2019 21:51
Deleted: , (13)

Revision 28/1/2019 21:51
Moved down [7]: ... [11]

Revision 28/1/2019 21:51
Deleted: 14a

Revision 28/1/2019 21:51
Deleted: 14b

Revision 28/1/2019 21:51
Deleted: 14c

Revision 28/1/2019 21:51
Deleted: 14b…2b) and (14c ... [12]

Revision 28/1/2019 21:51
Deleted: 15

Combining the constitutive expressions (Equation (3)), equilibrium condition (12a), strain-displacement relations (2) and displacement field (1), one obtains a second-order ordinary differential equation of which the solution for isotropic and transversely isotropic layers is [21]:

$$u_r^{(k)} = D^{(k)} r + E^{(k)} r^{-1}, \tag{14}$$

where $D^{(k)}$ and $E^{(k)}$ are unknown constants.

Under internal and external pressure, the boundary conditions at inner and outer radii are written as [21]:

$$\sigma_r^{(1)}(r_0) = -P_0, \quad \sigma_r^{(N)}(r_a) = -P_a, \tag{15a}$$

$$\tau_{\theta r}^{(1)}(r_0) = \tau_{zr}^{(1)}(r_0) = 0, \quad \tau_{\theta r}^{(N)}(r_a) = \tau_{zr}^{(N)}(r_a) = 0. \tag{15b}$$

Assuming perfectly bonded layers, the interface continuities are [20]:

$$u_r^{(k)}(r_k) = u_r^{(k+1)}(r_k), \quad u_\theta^{(k)}(r_k) = u_\theta^{(k+1)}(r_k), \tag{16a}$$

$$\sigma_r^{(k)}(r_k) = \sigma_r^{(k+1)}(r_k), \quad \tau_{\theta r}^{(k)}(r_k) = \tau_{\theta r}^{(k+1)}(r_k), \quad \tau_{zr}^{(k)}(r_k) = \tau_{zr}^{(k+1)}(r_k). \tag{16b}$$

Axial force at the pipe end is determined by integrating σ_z over the cross-sectional area and torque by the moment of $\tau_{z\theta}$. Considering a long pipe subjected to tension, axial equilibrium and zero torsion are expressed by the integrals [21]:

$$2\pi \sum_{k=1}^{N} \int_{r_{k-1}}^{r_k} \sigma_z^{(k)}(r) r \, \mathrm{d}r = F_A, \tag{17a}$$

$$2\pi \sum_{k=1}^{N} \int_{r_{k-1}}^{r_k} \tau_{z\theta}^{(k)}(r) r^2 \, \mathrm{d}r = 0. \tag{17b}$$

By substituting Equations (15b) and (16b) into (13), $A^{(k)} = B^{(k)} = 0$. For N layers there exist $2N+2$ unknowns, i.e. $D^{(k)}$, $E^{(k)}$, ε_0 and γ_0 (for $k = 1, 2, \ldots, N$), that can be determined from boundary conditions, continuity conditions and axial/torque integrals in order to obtain displacements, stresses and strains.

3. Lamina Failure Criteria

For assessing local stress-based material failure, stresses must be transformed from cylindrical to principal material coordinates as follows [21]:

$$\begin{Bmatrix} \sigma_1 \\ \sigma_2 \\ \sigma_3 \\ \tau_{23} \\ \tau_{13} \\ \tau_{12} \end{Bmatrix} = \begin{bmatrix} m^2 & n^2 & 0 & 0 & 0 & 2mn \\ n^2 & m^2 & 0 & 0 & 0 & -2mn \\ 0 & 0 & 1 & 0 & 0 & 0 \\ 0 & 0 & 0 & m & -n & 0 \\ 0 & 0 & 0 & n & m & 0 \\ -mn & mn & 0 & 0 & 0 & m^2 - n^2 \end{bmatrix} \begin{Bmatrix} \sigma_z \\ \sigma_\theta \\ \sigma_r \\ \tau_{\theta r} \\ \tau_{zr} \\ \tau_{z\theta} \end{Bmatrix}, \tag{18}$$

Revision 28/1/2019 21:51
Deleted: 14a

Revision 28/1/2019 21:51
Deleted: 16

Revision 28/1/2019 21:51
Deleted:

Revision 28/1/2019 21:51
Deleted: (r_a)

Revision 28/1/2019 21:51
Deleted: P_a, (17a

Revision 28/1/2019 21:51
Deleted: (r_a)

Revision 28/1/2019 21:51
Deleted: r_a

Revision 28/1/2019 21:51
Deleted: 17b

Revision 28/1/2019 21:51
Deleted: 18a

Revision 28/1/2019 21:51
Deleted: 18b

Revision 28/1/2019 21:51
Deleted: F_A, (19a

Revision 28/1/2019 21:51
Deleted: 19b

Revision 28/1/2019 21:51
Deleted: 17b

Revision 28/1/2019 21:51
Deleted: 18b

Revision 28/1/2019 21:51
Deleted: 15

Revision 28/1/2019 21:51
Formatted: Font:Not Italic

Revision 28/1/2019 21:51
Formatted: Font:Not Italic

Revision 28/1/2019 21:51
Formatted: Font:Italic

Revision 28/1/2019 21:51
Formatted: Font:Italic

Revision 28/1/2019 21:51
Deleted: (20

Revision 28/1/2019 21:51
Deleted:

Revision 28/1/2019 21:51
Moved (insertion) [7]

where $m = \cos\varphi$ and $n = \sin\varphi$.

In this study, the Maximum Stress (herein "Max Stress") and Tsai-Hill criteria are compared. According to Max Stress, failure is assumed simply when the stress along a principal direction exceeds the corresponding allowable, i.e. when any of the following are exceeded:

$$-X_C < \sigma_1 < X_T, \quad -Y_C < \sigma_2 < Y_T, \quad -Z_C < \sigma_3 < Z_T,$$

$$|\tau_{23}| < Q, \quad |\tau_{13}| < R, \quad |\tau_{12}| < S, \tag{19}$$

where X, Y and Z are tensile or compressive strengths (subscripts 'T' and 'C') along directions 1, 2 and 3 respectively; Q, R and S are the shear strengths in coordinates 23, 13 and 12 respectively. Interaction amongst stresses within a lamina is unaccounted for, which can result in error for multi-axial cases. Stress interaction is accounted for in the widely used quadratic Tsai-Hill criterion, expressed as:

$$\frac{\sigma_1^2}{X_T^2} + \frac{\sigma_2^2}{Y_T^2} + \frac{\sigma_3^2}{Z_T^2} - \sigma_1\sigma_2\left(\frac{1}{X_T^2} + \frac{1}{Y_T^2} - \frac{1}{Z_T^2}\right) - \sigma_1\sigma_3\left(\frac{1}{X_T^2} - \frac{1}{Y_T^2} + \frac{1}{Z_T^2}\right) - \sigma_2\sigma_3\left(-\frac{1}{X_T^2} + \frac{1}{Y_T^2} + \frac{1}{Z_T^2}\right) + \frac{\tau_{23}^2}{Q^2} + \frac{\tau_{13}^2}{R^2} + \frac{\tau_{12}^2}{S^2} = 1. \tag{20}$$

4. Numerical Simulation

4.1. TCP Mechanical Model

A 3D FE model was developed in Abaqus/CAE 2017 capable of predicting stress state in a section of TCP under combined pressures, tension and thermal gradient. Dimensions of the 'basic' configuration modelled for this study are given in Table 1. The inner liner, laminate and outer liner of the basic TCP are an equal thickness of 8mm, which we denote here as "8:8:8". In this study, the liner thicknesses are varied with respect to the laminate, for example 4:8:4 (equally thick liners), or 4:8:12 (unequal liners). The laminate is constructed of eight FW layers orientated in the sequence $[\pm 55]_4$, each wound to a thickness of 1mm.

Table 1. Basic TCP section dimensions

Dimension	Value
Inner radius, r_0 (mm)	76
Inner liner thickness, t_{in} (mm)	8
Laminate thickness, t_{lam} (mm)	8
Outer liner thickness, t_{out} (mm)	8
Outer radius, r_a (mm)	100

The TCP consists of unidirectional AS4/APC-2 carbon/PEEK laminate plies and homogeneous APC-2 PEEK liners. APC-2 PEEK composite has a glass transition temperature (T_g) of 143°C and can be used in lightly loaded applications at temperatures as high as 260°C [23]. Properties used to define the materials over a range of temperatures are given in Tables 2 and 3, where data has been carefully compiled as far as possible from literature. To the authors' best knowledge these tables represent the most comprehensive compilation of AS4/APC-2 properties over the relevant temperature range. Note that for practical application the designer should always assess properties of the specific chosen material

Revision 28/1/2019 21:51
Deleted: $X_C X_C < \sigma_1 < X_T$ ... [13]
Revision 28/1/2019 21:51
Deleted: $Y_C Y_C < \sigma_2 < Y_T$ ... [14]
Revision 28/1/2019 21:51
Deleted: $Z_C Z_C < \sigma_3 < Z_T$ ... [15]
Revision 28/1/2019 21:51
Deleted: 21
Revision 28/1/2019 21:51
Deleted: *T*…T' and *C* ... [16]
Revision 28/1/2019 21:51
Formatted ... [17]
Revision 28/1/2019 21:51
Deleted: $\frac{\sigma_1^2}{X_T^2}$
Revision 28/1/2019 21:51
Deleted: $\frac{\sigma_2^2}{Y_T^2}\frac{\sigma}{Y}\frac{2}{2} + \frac{\sigma_3^2}{Z_T^2}\frac{\sigma}{Z}\frac{3}{2} -$ ... [18]
Revision 28/1/2019 21:51
Deleted: 22
Revision 28/1/2019 21:51
Deleted:
Revision 28/1/2019 21:51
Deleted: on…n Abaqus/CAE 2017 ... [19]
Revision 28/1/2019 21:51
Deleted:
Revision 28/1/2019 21:51
Formatted: Font:Not Italic
Revision 28/1/2019 21:51
Deleted: t_i
Revision 28/1/2019 21:51
Deleted: t_l
Revision 28/1/2019 21:51
Deleted: t_o
Revision 28/1/2019 21:51
Formatted: Font:Not Italic
Revision 28/1/2019 21:51
Deleted: 22

experimentally. The following assumptions are made to fully define the AS4/APC-2 for temperature dependent analysis:

- Properties listed in Tables 2 and 3 are linearly inter/extrapolated over the temperature range considered in this study (which is below T_g).
- Poisson's ratio v_{23} at room temperature (RT) [26] is assumed to increase by 2.7% at 121°C as per reported data for v_{12} and v_{13} [25].
- Shear modulus G_{23} is calculated as:

$$G_{23} = \frac{E_2}{2(1 + v_{23})}.$$

- Shear strength Q at RT [26] is assumed to reduce by 14.5% and 22.0% at 82°C and 121°C respectively as per reported data for R and S [23].
- It is assumed that thermal expansion coefficients remain unchanged over the temperature range investigated in this study.

Table 2. Unidirectional AS4/APC-2 properties

Property	**RT (23-24°C)**	**66°C**	**82°C**	**100°C**	**121°C**
E_1 (GPa) [24]	142	-	-	131	-
$E_2 = E_3$ (GPa) [24]	9.6	-	-	8.6	-
$G_{12} = G_{13}$ (GPa) [24]	6.0	-	-	4.8	-
G_{23} (GPa)	3.6*	-	-	3.2*	-
$v_{12} = v_{13}$ [25]	0.37	-	-	-	0.38
v_{23} [26]	0.33	-	-	-	0.34^{+}
α_1 (°C^{-1}) [26]	-0.18x10^{-6}	-	-	-	-
$\alpha_2 = \alpha_3$ (°C^{-1}) [26]	23.94x10^{-6}	-	-	-	-
λ_1 (Wm^{-1}°C^{-1}) [27]	4.0	4.35	4.5	4.60	4.8
$\lambda_2 = \lambda_3$ (Wm^{-1}°C^{-1}) [27]	0.43	0.46	0.48	0.50	0.53
X_T (MPa) [24]	2070	-	-	2008	-
$Y_T = Z_T$ (MPa) [24]	79	-	-	66	-
X_C (MPa) [28]	1234	1036	-	-	985
$Y_C = Z_C$ (MPa) [28]	176	163	-	-	136
Q (MPa) [26]	92	-	78.7^{+}	-	71.8^{+}
$R = S$ (MPa) [23]	186	-	159	-	145

*Calculated value; $^{+}$Estimated value

Table 3. Neat APC-2 PEEK properties

Property	**0°C**	**RT (23-24°C)**	**60°C**	**82°C**	**100°C**	**121°C**
E (GPa) [24]	-	4.1	-	3.8	-	3.5
v [24]	-	0.41	-	0.44	-	0.44
α (°C^{-1}) [24]	-	50.8x10^{-6}	-	-	-	-
λ (Wm^{-1}°C^{-1}) [29]	0.27	0.28	0.30	0.30	0.31	0.32
σ_N (MPa) [30]	119	106	76	-	51.77^{+}	-

$^{+}$Estimated value

Deleted: 25
Revision 28/1/2019 21:51
Formatted ... [20]
Revision 28/1/2019 21:51
Deleted: 24
Revision 28/1/2019 21:51
Formatted ... [21]
Revision 28/1/2019 21:51
Formatted ... [22]
Revision 28/1/2019 21:51
Deleted: . ... [23]
Revision 28/1/2019 21:51
Deleted: CTEs
Revision 28/1/2019 21:51
Formatted ... [24]
Revision 28/1/2019 21:51
Deleted: 23
Revision 28/1/2019 21:51
Formatted ... [25]
Revision 28/1/2019 21:51
Deleted: 23
Revision 28/1/2019 21:51
Formatted ... [26]
Revision 28/1/2019 21:51
Deleted: 23
Revision 28/1/2019 21:51
Formatted ... [27]
Revision 28/1/2019 21:51
Deleted: 24
Revision 28/1/2019 21:51
Formatted ... [28]
Revision 28/1/2019 21:51
Formatted ... [29]
Revision 28/1/2019 21:51
Deleted: 25
Revision 28/1/2019 21:51
Formatted ... [30]
Revision 28/1/2019 21:51
Deleted: 25
Revision 28/1/2019 21:51
Formatted ... [31]
Revision 28/1/2019 21:51
Deleted: 25
Revision 28/1/2019 21:51
Formatted ... [32]
Revision 28/1/2019 21:51
Deleted: 26
Revision 28/1/2019 21:51
Formatted ... [33]
Revision 28/1/2019 21:51
Deleted: 26
Revision 28/1/2019 21:51
Formatted ... [34]
Revision 28/1/2019 21:51
Deleted: 23
Revision 28/1/2019 21:51
Formatted ... [35]
Revision 28/1/2019 21:51
Deleted: 23
Revision 28/1/2019 21:51
Deleted: 27
Revision 28/1/2019 21:51
Formatted ... [36]
Revision 28/1/2019 21:51
Formatted ... [37]
Revision 28/1/2019 21:51
Revision 28/1/2019 21:51
Revision 28/1/2019 21:51
Revision 28/1/2019 21:51
Revision 28/1/2019 21:51
Revision 28/1/2019 21:51

Internal and external surface pressures are applied simultaneously, along with axial tension, applied as a point load on a reference point located at the centre of one pipe end and fully coupled to the end face in all but the radial direction, as shown in Figure 4. At the opposite pipe end, a reference point is fully fixed in the centre and coupled to the end face.

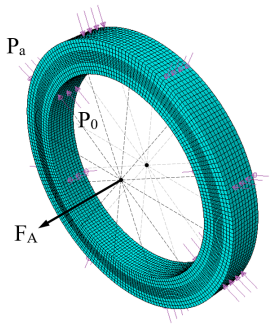

Figure 4. Axial point load and kinematic coupling

4.2. Validation of the Mechanical Model

The model was firstly validated for the case of combined pressure and tension prior to extending to include thermal load and defining temperature dependent properties on Abaqus. An analytical solution based on the Section 2 formulation excluding thermal component was developed in MATLAB for comparison with the FE model. Analysis was run for "A" and "B" TCP configurations with different laminate ply sequences (the basic $[\pm 55]_4$ and $[(\pm 15)_2/(90)_4]$ respectively) to validate fibre angle orientation under the following load conditions: P_0 = 40MPa; P_a = 20MPa; F_A = 50kN.

Through-thickness cylindrical stresses based on the MATLAB and FE models are shown in Figure 5. For both configurations MATLAB and Abaqus strongly agree. The Abaqus model was extended to thermomechanical by creating a coupled temperature-displacement step and employing appropriate thermal elements (C3D20RT). A suitable mesh was established by performing a refinement exercise.

Revision 28/1/2019 21:51
Deleted: .

Revision 28/1/2019 21:51
Deleted:

Revision 28/1/2019 21:51
Deleted: on

Revision 28/1/2019 21:51
Formatted: Font:Not Italic

Revision 28/1/2019 21:51
Formatted: Font:Not Italic

Revision 28/1/2019 21:51
Formatted: Font:Not Italic

Revision 28/1/2019 21:51
Deleted: 4

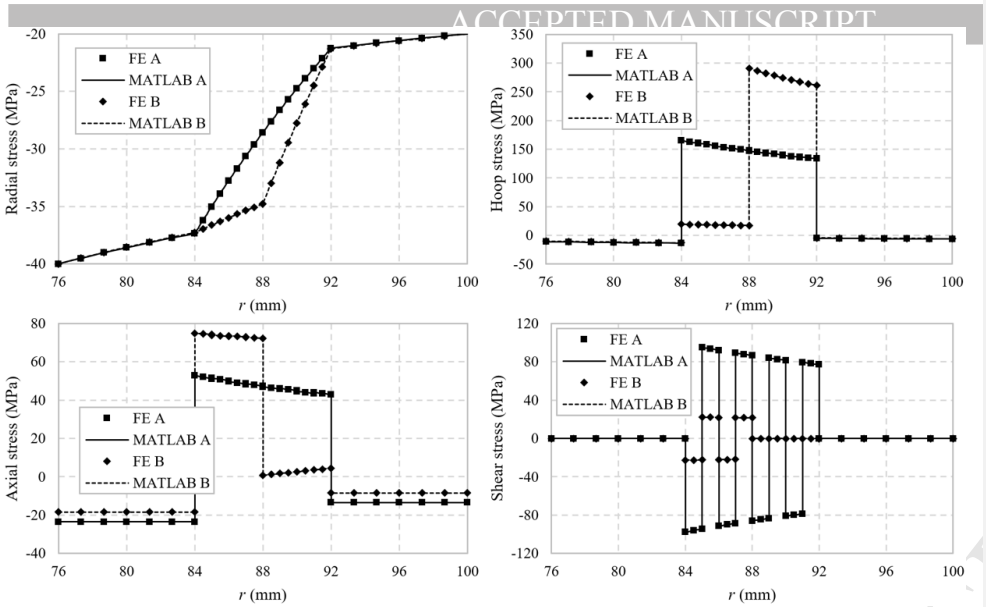

Figure 5. Validation of FE model stresses

4.3. Thermal Loading

During its service life, the internal temperature of a riser may vary considerably whereas the external seawater temperature will remain near constant in deepwater. In this study, increasing temperatures are applied as fixed boundary conditions on the internal surface. On the outer surface, a film coefficient is applied to simulate free convection to the surrounding environment.

5. Results and Discussion

Simulations were run for TCP under combined pressures, axial tension and thermal gradient illustrative of an SLHR operating in ultra deepwater (1,500m and beyond). In all cases internal pressure, external pressure and tension of 40MPa, 20MPa and 50kN respectively were applied (illustrative of operation at around 2,000m depth). Internal surface temperature was increased from 30 to 120°C to investigate the effects of increasing through-thickness gradient. The surrounding seawater temperature was 4°C with a heat transfer coefficient of 50$Wm^{-2}°C^{-1}$. An initial temperature of 23°C for the TCP was assumed.

5.1. Effects of Increasing Thermal Gradient

Through-thickness temperature distributions for the basic TCP (Table 1 configuration with $[\pm 55]_4$ laminate) under rising internal temperature are shown in Figure 6. Temperature decreases linearly from internal to external surfaces at different rates through the layers. The slope is steeper through the liners (r = 76 to 84mm, 92 to 100mm) than the laminate, owing to lower thermal conductivity and thus greater insulating characteristics. The temperature variation through the laminate increases with T_0. The outer surface temperature as a result of heat convection is 8.9 and 27.1°C for T_0 = 30 and 120°C respectively.

Revision 28/1/2019 21:51
Deleted: 4

Revision 28/1/2019 21:51
Deleted:

Revision 28/1/2019 21:51
Deleted: a

Revision 28/1/2019 21:51
Deleted: SLHR application.

Revision 28/1/2019 21:51
Deleted: 3

Revision 28/1/2019 21:51
Deleted: 5

Revision 28/1/2019 21:51
Formatted: Font:Not Italic

Revision 28/1/2019 21:51
Formatted: Font:Not Italic

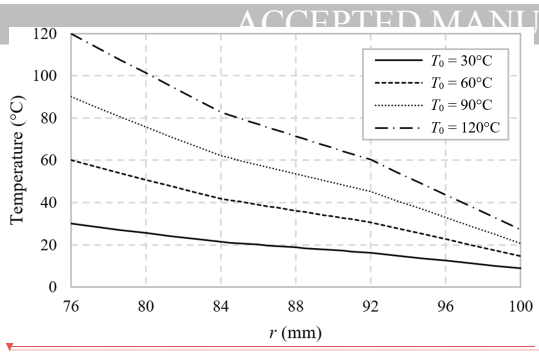

Figure 6. Temperature distributions for increasing T_0: basic TCP

Stress variations through the basic TCP under increasing T_0 are shown in Figure 7. Radial stress (σ_r) magnitude decreases linearly from the value of internal pressure on the inner surface to external pressure at the outer surface through the layers. Hoop (σ_θ), axial (σ_z) and shear ($\tau_{z\theta}$) stresses are predominantly carried by the laminate and increase with temperature gradient. The sign of the shear stress alternates with each ±55° ply.

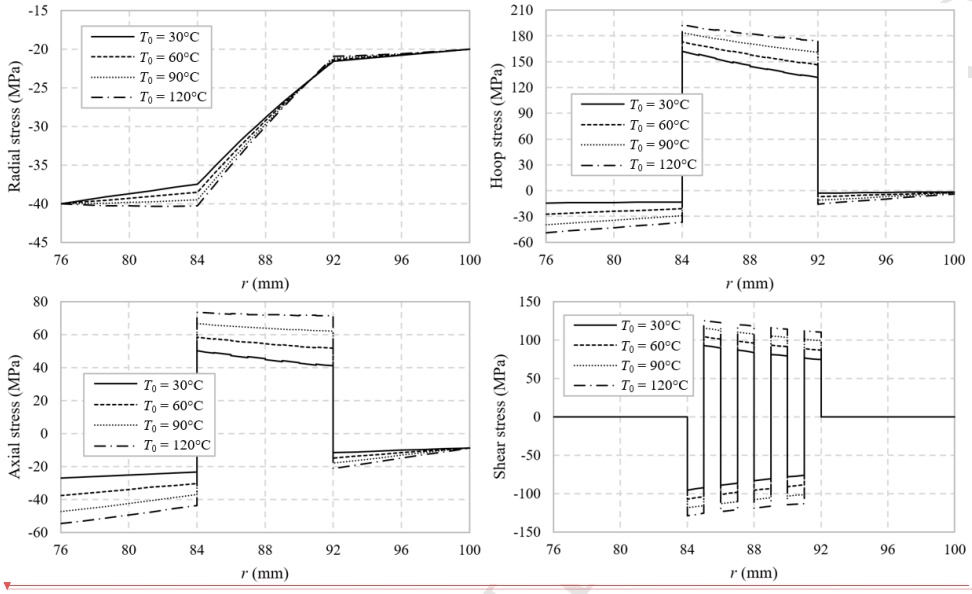

Figure 7. Stress variation in the basic TCP for increasing T_0

Von Mises failure coefficients through the liners are shown in Figure 8. The coefficient is generally smaller through the inner liner at increased T_0. In the outer liner, the coefficient decreases at r = 92mm with rising T_0 but is virtually unaltered at r_a. Failure coefficients through the laminate according to Max Stress and Tsai-Hill are shown in Figure 9. The Max Stress coefficient, governed by the compressive stress-to-strength ratio in the radial direction, increases slightly with T_0 at r = 84mm but is gradually less altered towards r = 92mm. This reflects the radial stress distributions in Figure 7, which are near identical for all T_0 towards r = 92mm. As per Max Stress, the interactive Tsai-Hill coefficient is also largest at r =

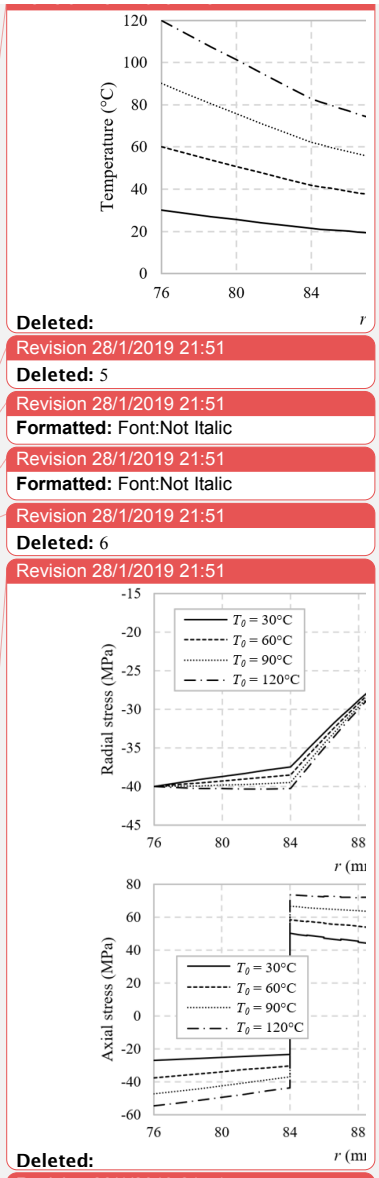

Deleted:

Revision 28/1/2019 21:51
Deleted: 5

Revision 28/1/2019 21:51
Formatted: Font:Not Italic

Revision 28/1/2019 21:51
Formatted: Font:Not Italic

Revision 28/1/2019 21:51
Deleted: 6

Revision 28/1/2019 21:51

Deleted:

Revision 28/1/2019 21:51
Deleted: 6

Revision 28/1/2019 21:51
Formatted: Font:Not Italic

Revision 28/1/2019 21:51
Deleted: 7…. The coefficient is gen ... [39]

Revision 28/1/2019 21:51
Formatted ... [40]

Revision 28/1/2019 21:51
Deleted: 8

Revision 28/1/2019 21:51
Formatted: Font:Not Italic

Revision 28/1/2019 21:51
Deleted: 6

Revision 28/1/2019 21:51
Formatted: Font:Not Italic

84mm for all cases. However, the increase with thermal gradient is uniform through the thickness, albeit marginal. The non-interactive simplistic nature of Max Stress is known to result in potential inaccuracies when predicting failure.

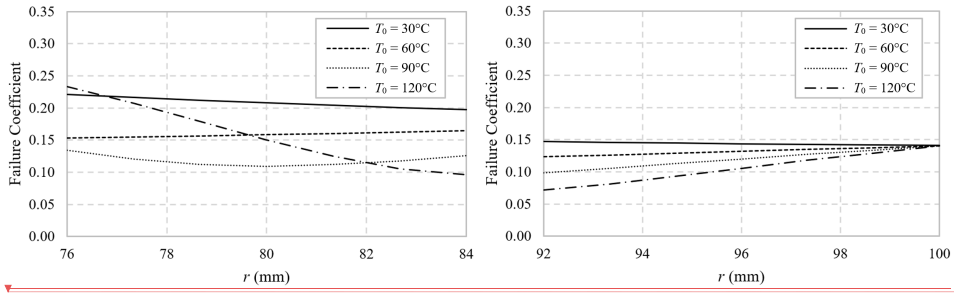

Figure 8. Von Mises coefficient through inner (left) and outer liner (right) for increasing T_0: basic TCP

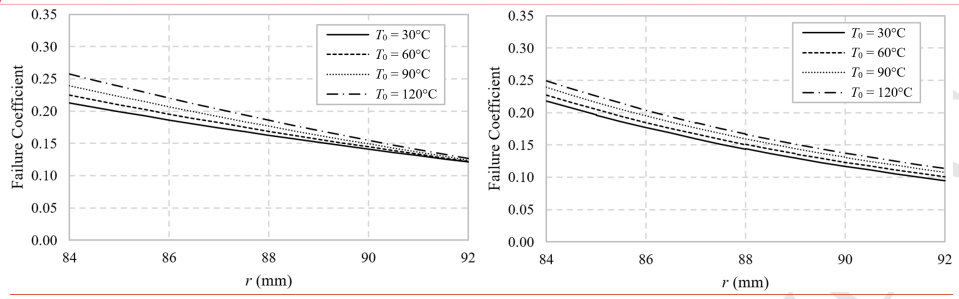

Figure 9. Through-laminate Max Stress (left) and Tsai-Hill coefficient (right) for increasing T_0: basic TCP

5.2. Effects of Varying Liner Thickness

Here, we investigate the effects of varying the thickness of the liners concurrently with respect to the laminate, the dimensions of which are kept constant. Temperature distributions for 4mm thick liner (4:8:4) and 12mm thick liner (12:8:12) configurations are shown in Figure 10. At higher gradients, the laminate temperature is hotter with thin liners and the difference through the laminate thickness is greater. The drop in temperature through the 4:8:4 laminate is almost double that of the 12:8:12, dropping from 94.2 to 62.5°C compared to 75.9 to 58.5°C. Thicker liners effectively regulate the temperature variation through the central laminate.

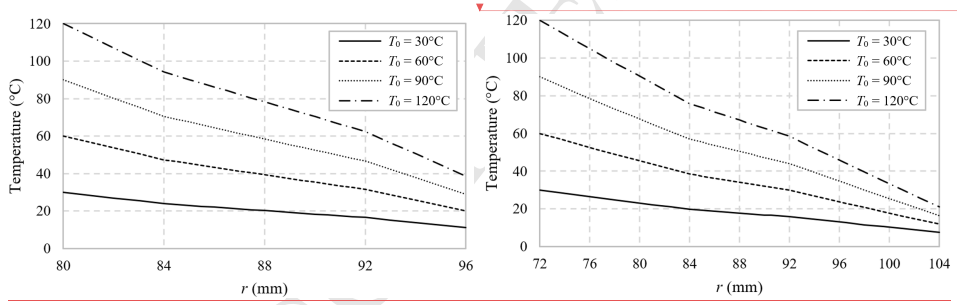

Revision 28/1/2019 21:51
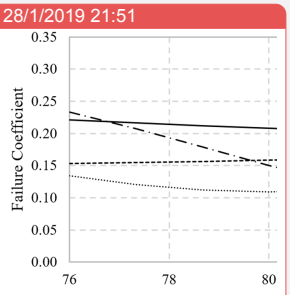

Deleted:
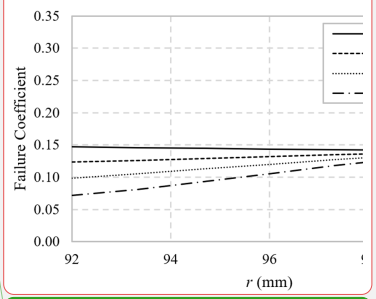

Revision 28/1/2019 21:51
Moved (insertion) [8]

Revision 28/1/2019 21:51
Formatted: Font:Not Italic

Revision 28/1/2019 21:51
Deleted: ... [41]

Revision 28/1/2019 21:51
Moved up [8]: Figure 8.

Revision 28/1/2019 21:51
Formatted: Font:Not Italic

Revision 28/1/2019 21:51
Deleted: 9

Revision 28/1/2019 21:51
Deleted: ... [42]

Figure 10. Temperature distributions for increasing T_0: 4:8:4 (left) and 12:8:12 (right)

Von Mises coefficients through 4mm and 12mm liners are shown in Figure 11. The coefficient increases significantly in the 4mm inner liner at the highest T_0 but varies only slightly in the 4mm outer liner with T_0. On the other hand, the coefficient is smaller for the inner 12mm liner at higher thermal gradients and becomes highly nonlinear at T_0 = 120°C. The coefficient decreases in the outer 12mm liner with rising thermal gradient but for a small increase towards r_o. At higher thermal gradients, thicker liners are superior in terms of affording higher practical safety factor, particularly in the inner liner. As can be seen in Figure 10, the differences in temperature between load cases are greatest in the inner liner, which result in more drastic variation of the failure coefficient with increasing T_0.

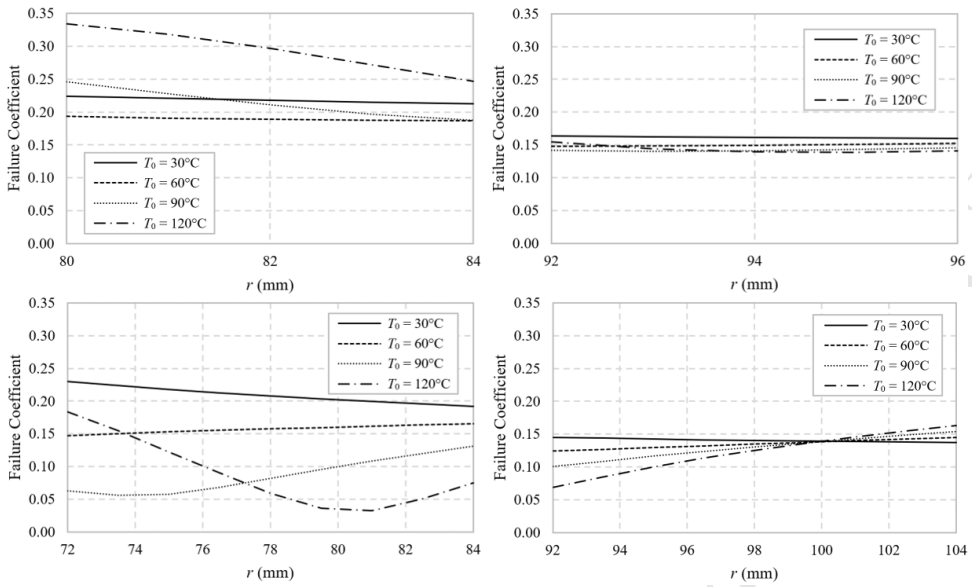

Figure 11. Von Mises coefficient through inner (left) and outer liner (right) for increasing T_0: 4:8:4 (top) and 12:8:12 (bottom)

4:8:4 and 12:8:12 through-laminate Max Stress and Tsai-Hill distributions are shown in Figures 12 and 13. The Max Stress coefficient decreases bilinearly through the 4:8:4 laminate, as the governing failure mode switches from radial compression in the innermost plies to in-plane shear in the outermost. In the case of 12mm liners, the coefficient is governed entirely by radial compression and with rising T_0 the largest increase is observed at r = 84mm, as we have earlier seen. The Tsai-Hill coefficient decreases slightly with rising T_0 through the 4:8:4 laminate. Conversely, the coefficient increases significantly for the 12:8:12 configuration. For the 12mm liner configuration, the Max Stress criterion significantly under-predicts failure compared to Tsai-Hill.

Revision 28/1/2019 21:51
Deleted: 9

Revision 28/1/2019 21:51
Formatted: Font:Not Italic

Revision 28/1/2019 21:51
Deleted: 10

Revision 28/1/2019 21:51
Formatted: Font:Not Italic

Revision 28/1/2019 21:51
Deleted: . In the 4mm outer liner, the coefficient

Revision 28/1/2019 21:51
Deleted: very

Revision 28/1/2019 21:51
Deleted: thermal gradient.

Revision 28/1/2019 21:51
Deleted: value decreases through both

Revision 28/1/2019 21:51
Deleted: liners

Revision 28/1/2019 21:51
Deleted: (with

Revision 28/1/2019 21:51
Deleted: exception

Revision 28/1/2019 21:51
Formatted: Font:Not Italic

Revision 28/1/2019 21:51
Deleted:).

Revision 28/1/2019 21:51
Deleted: . ... [43]

Revision 28/1/2019 21:51
Formatted: Font:Not Italic

Revision 28/1/2019 21:51
Deleted: 11

Revision 28/1/2019 21:51
Deleted: 12

Revision 28/1/2019 21:51
Formatted: Font:Not Italic

Revision 28/1/2019 21:51
Formatted: Font:Not Italic

Revision 28/1/2019 21:51
Formatted: Left, Indent: First line: 0 cm

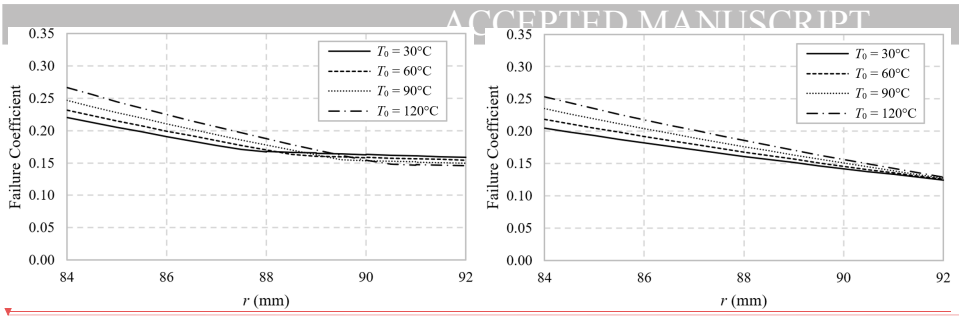

Figure 12. Through-laminate Max Stress coefficient for increasing T_0: 4:8:4 (left) and 12:8:12 (right)

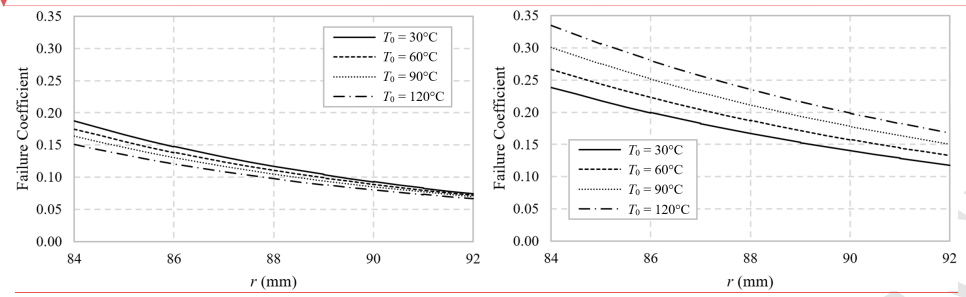

Figure 13. Through-laminate Tsai-Hill coefficient for increasing T_0: 4:8:4 (left) and 12:8:12 (right)

In summary, for the TCP considered here, von Mises failure coefficient in a thin inner liner increases with rising thermal gradient but laminate failure is not significantly altered, whereas thick liners are less prone to failure at higher gradients but the Tsai-Hill coefficient increases uniformly and substantially through the laminate with thick liners. Recalling that the liner primary function is to provide fluid tightness and wear resistance, the implications of using thin liners must be assessed e.g. for cracking.

5.3. Comparison of Thick Inner or Outer Liner

In this section, we investigate the failure response of a configuration with thin inner and thick outer liner, and vice versa, as opposed to liners of equal thickness. Von Mises coefficients through 4:8:12 and 12:8:4 configuration liners are shown in Figure 14. The coefficient is largest through the thick inner liner at T_0 = 30°C. For the thin inner liner, the coefficient is largest at r_0 for the T_0 = 120°C case. In both cases the outer liner coefficient is largest for the smallest T_0. The coefficient exhibits nonlinear behaviour in both thick liners at high thermal gradient. As before, the effects of rising gradient are greatest in the inner liner, regardless of whether a thin inner and thick outer liner or vice versa is used.

Revision 28/1/2019 21:51
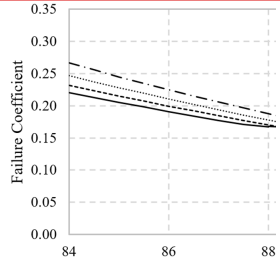

Deleted: ... [44]

Revision 28/1/2019 21:51
Deleted: 11

Revision 28/1/2019 21:51
Formatted: Font:Not Italic

Revision 28/1/2019 21:51
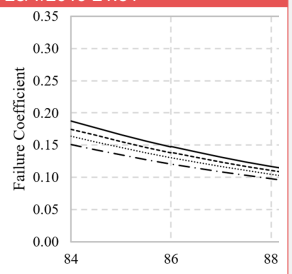

Deleted: ... [45]

Revision 28/1/2019 21:51
Deleted: 12

Revision 28/1/2019 21:51
Formatted: Font:Not Italic

Revision 28/1/2019 21:51
Deleted: laminate …onsidered here, ... [46]

Revision 28/1/2019 21:51
Deleted: 13…4. The coefficient ... [47]

Revision 28/1/2019 21:51
Formatted: Font:Not Italic

Revision 28/1/2019 21:51
Deleted: decreases …s largest at r_0 f ... [48]

Revision 28/1/2019 21:51
Formatted: Font:Not Italic

Revision 28/1/2019 21:51
Formatted: Font:+Theme Body, 12 pt

Revision 28/1/2019 21:51
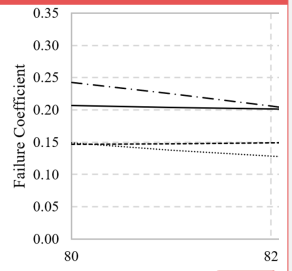

Deleted: ... [49]

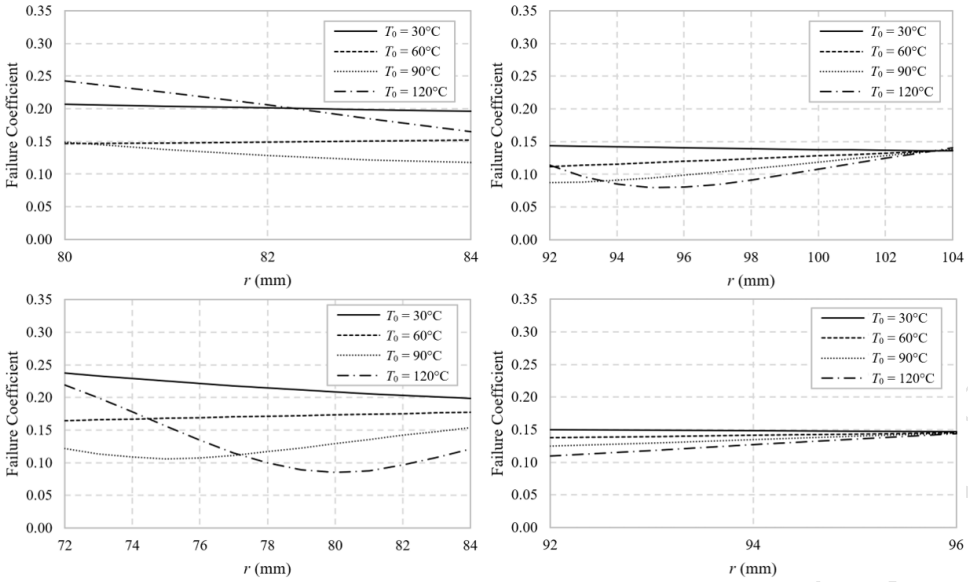

Figure 14. Von Mises coefficient through inner (left) and outer liner (right) for increasing T_0: 4:8:12 (top) and 12:8:4 (bottom)

Tsai-Hill coefficients through the 4:8:12 and 12:8:4 laminates are shown in Figure 15. At T_0 = 30°C the coefficients for both cases are near identical. The coefficient increases greatly with rising T_0 for the 12:8:4 configuration but remains virtually unchanged for the 4:8:12 case. From a practical point-of-view, for the same overall TCP thickness a thin inner and thick outer liner (4:8:12) is superior to the opposite configuration in terms of lower predicted Tsai-Hill laminate failure and only slightly greater liner von Mises coefficient at high thermal gradient.

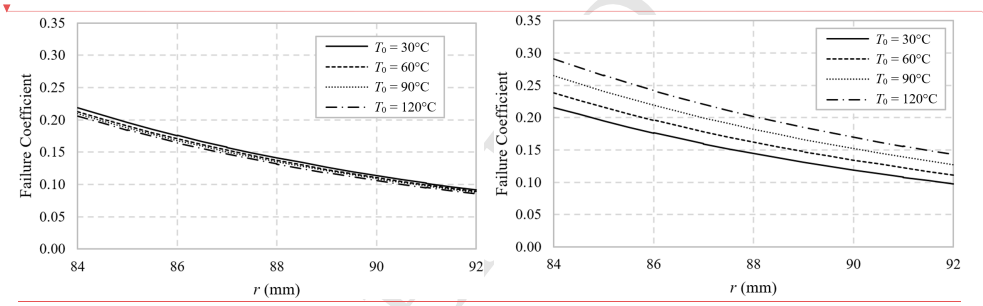

Figure 15. Through-laminate Tsai-Hill coefficient for increasing T_0: 4:8:12 (left) and 12:8:4 (right)

5.4. Discussion

Revision 28/1/2019 21:51
Deleted: 13

Revision 28/1/2019 21:51
Formatted: Font:Not Italic

Revision 28/1/2019 21:51
Deleted: 14

Revision 28/1/2019 21:51
Formatted: Font:Not Italic

Revision 28/1/2019 21:51
Formatted: Font:Not Italic

Revision 28/1/2019 21:51
Deleted: ... [50]

Revision 28/1/2019 21:51
Deleted: 14

Revision 28/1/2019 21:51
Formatted: Font:Not Italic

In the scenarios investigated, the laminate Tsai-Hill coefficient was lowest for the TCP with thin (4mm) liners. However, large liner failure coefficient was observed, particularly in the inner liner at high thermal gradient. As opposed to utilising two thick (12mm) liners, which are less prone to failure but cause a substantial rise in laminate Tsai-Hill coefficient, an optimal design can be achieved by utilising a thin inner and thick outer liner. In this case, laminate Tsai-Hill coefficient is lower and more stable at temperature, and the liner von Mises coefficient is only marginally higher than the opposite configuration with the same overall thickness. A thick outer liner also offers enhanced resistance to external wear and tear. However, the designer should consider the implications of a larger outer radius, e.g. in terms of bend radius (for spooling) and external fluid mechanics. The local material failure model presented can be used in conjunction with global riser analysis tools for global-local analysis.

This study has highlighted the importance of considering varying internal operating temperature for the practical application of TCP risers. High internal-to-external thermal gradient may lead to highly nonlinear effects in failure coefficients through thick liners, particularly a thick inner liner. The inner liner will experience larger changes in temperature during deepwater operation than the outer liner and the effects of rising internal temperature on failure coefficient are greater regardless of whether the inner liner is thinner or thicker than the outer. Appropriate optimisation of liner thickness can regulate the extent to which the laminate failure coefficient changes with varying internal operating temperature.

6. Conclusions

In this paper, a 3D FE model was developed to analyse stress state in TCP under combined pressure, tension and thermal gradient considering temperature-dependent material properties. From obtained stresses, through-thickness failure coefficient was analysed according to von Mises through isotropic liners and Max Stress and Tsai-Hill criteria through the laminate for illustrative SLHR load cases. The internal surface temperature was increased to investigate rising internal-to-external thermal gradient.

The effects of varying the liner thickness with respect to the central laminate were examined. In practical terms, varying the liner thickness creates a trade-off between liner and laminate safety factor as the thermal gradient is increased. Tsai-Hill coefficient through a laminate with equally thin liners does not change significantly with thermal gradient, however the von Mises failure coefficient in the inner liner increases considerably. On the other hand, equally thick liners are not more prone to yielding at increased thermal gradients but interactive failure coefficient of the central laminate increases.

For the TCP considered here, a thin inner and thick outer liner is superior to the opposite configuration in terms of lower laminate Tsai-Hill failure coefficient. Whilst this configuration appears optimal for the studied operating conditions, the designer should consider the implications, e.g. in terms of through-liner cracking, external fluid mechanics and bending of the pipe during transportation and installation. Global riser analysis tools can be used to determine the inputs for the TCP failure model presented here, i.e. to perform global-local analysis.

Acknowledgements

The authors wish to thank Dr Oleksandr Menshykov and Dr Maryna Menshykova of the Centre for Micro- and Nanomechanics, University of Aberdeen, for providing MATLAB script for validation purposes.

Revision 28/1/2019 21:51
Deleted: at

Revision 28/1/2019 21:51
Formatted: Font:12 pt, Bold

References

[1] Guz, I.A., Menshykova, M., Paik, J.K., 2017. Thick-walled composite tubes for offshore applications: an example of stress and failure analysis for filament-wound multi-layered pipes. Ships and Offshore Structures 12 (3), 304-322.

[2] Menshykova, M., Guz, I.A., 2014. Stress analysis of layered thick-walled composite pipes subjected to bending loading. International Journal of Mechanical Sciences 88, 289-299.

[3] Bai, Y., Wang, N., Cheng, P., Qiao, H., Yu, B., 2015. Collapse and buckling behaviors of reinforced thermoplastic pipe under external pressure. Journal of Offshore Mechanics and Arctic Engineering 137 (4), 041401.

[4] Kruijer, M.P., Warnet, L.L., Akkerman, R., 2005. Analysis of the mechanical properties of a reinforced thermoplastic pipe (RTP). Composites Part A: Applied Science and Manufacturing 36 (2), 291-300.

[5] Ashraf, M.A., Morozov, E.V., Shankar, K., 2014. Flexure analysis of spoolable reinforced thermoplastic pipes for offshore oil and gas applications. Journal of Reinforced Plastics and Composites 33 (6), 533-542.

[6] Yu, K., Morozov, E.V., Ashraf, M.A., Shankar, K., 2015. Analysis of flexural behaviour of reinforced thermoplastic pipes considering material nonlinearity. Composite Structures 119, 385-393.

[7] Yu, K., Morozov, E.V., Ashraf, M.A., Shankar, K., 2015. Numerical analysis of the mechanical behaviour of reinforced thermoplastic pipes under combined external pressure and bending. Composite Structures 131, 453-461.

[8] Bai, Y., Xu, W., Cheng, P., Wang, N., Ruan, W., 2014. Behaviour of reinforced thermoplastic pipe (RTP) under combined external pressure and tension. Ships and Offshore Structures 9 (4), 464-474.

[9] Bai, Y., Ruan, W., Cheng, P., Yu, B., Xu, W., 2014. Buckling of reinforced thermoplastic pipe (RTP) under combined bending and tension. Ships and Offshore Structures 9 (5), 525-539.

[10] Li, G.H., Wang, W.J., Jing, Z.J., Ma, X.C., Zuo, L.B., 2016. Experimental Study and Finite Element Analysis of Critical Stresses of Reinforced Thermoplastic Pipes Under Various Loads. Strength of Materials 48 (1), 165-172.

[11] Kruijer, M.P., Warnet, L.L., Akkerman, R., 2006. Modelling of the viscoelastic behaviour of steel reinforced thermoplastic pipes. Composites Part A: Applied Science and Manufacturing 37 (2), 356-367.

[12] Xia, M., Kemmochi, K., Takayanagi, H., 2001. Analysis of filament-wound fiber-reinforced sandwich pipe under combined internal pressure and thermomechanical loading. Composite Structures 51 (3), 273-283.

[13] Akçay, İ.H., Kaynak, İ., 2005. Analysis of multilayered composite cylinders under thermal loading. Journal of Reinforced Plastics and Composites 24 (11), 1169-1179.

[14] Bakaiyan, H., Hosseini, H., Ameri, E., 2009. Analysis of multi-layered filament-wound composite pipes under combined internal pressure and thermomechanical loading with thermal variations. Composite Structures 88 (4), 532-541.

[15] Zhang, Q., Wang, Z.W., Tang, C.Y., Hu, D.P., Liu, P.Q., Xia, L.Z., 2012. Analytical solution of the thermo-mechanical stresses in a multilayered composite pressure vessel considering the influence of the closed ends. International Journal of Pressure Vessels and Piping 98, 102-110.

[16] Wang, L., Zheng, C., Wei, S., Wei, Z., 2016. Micromechanics-based progressive failure analysis of carbon fiber/epoxy composite vessel under combined internal pressure and thermomechanical loading. Composites Part B: Engineering 89, 77-84.

[17] Vedeld, K., Sollund, H.A., 2014. Stresses in heated pressurized multi-layer cylinders in generalized plane strain conditions. International Journal of Pressure Vessels and Piping, 120-121, 27-35.

[18] Sollund, H.A., Vedeld, K., Hellesland, J., 2014. Efficient analytical solutions for heated and pressurized multi-layer cylinders. Ocean Engineering, 92, 285-295.

[19] Yeo, W.H., Purbolaksono, J., Aliabadi, M.H., Ramesh, S., Liew, H.L., 2017. Exact solution for stresses/displacements in a multilayered hollow cylinder under thermo-mechanical loading. International Journal of Pressure Vessels and Piping 151, 45-53.

[20] Xia, M., Takayanagi, H., Kemmochi, K., 2001. Analysis of multi-layered filament-wound composite pipes under internal pressure. Composite Structures 53 (4), 483-491.

[21] Herakovich, C.T., 1998. Mechanics of fibrous composites. New York (NY): Wiley.

[22] Haji-Sheikh, A., Beck, J.V., Agonafer, D., 2003. Steady-state heat conduction in multi-layer bodies. International Journal of Heat and Mass Transfer 46 (13), 2363-2379.

[23] Cytec, 2012. APC-2 PEEK thermoplastic polymer technical data sheet.

[24] Coquill, S.L., Adams, D.F., 1989. Mechanical properties of several neat polymer matrix materials and unidirectional carbon fiber-reinforced composites. NASA CR-181805.

[25] Ramey, J. and Palazotto, A.,1989. A study of graphite/PEEK under high temperatures. G.M. Newaz, ed., Advances in Thermoplastic Matrix Composite Materials. Chelsea (MI): ASTM, 91-112.

[26] Yousefpour, A., Nejhad, M.N.G., 2004. Design, analysis, manufacture, and test of APC-2/AS4 thermoplastic composite pressure vessels for deep water marine applications. Journal of Composite Materials 38 (19), 1701-1732.

Revision 28/1/2019 21:51
Deleted: [22

Revision 28/1/2019 21:51
Deleted: 23

Revision 28/1/2019 21:51
Deleted: 24

Revision 28/1/2019 21:51
Deleted: 25

[27] Grove, S.M., 1988. Thermal modelling of tape laying with continuous carbon fibre-reinforced thermoplastic. Composites 19 (5), 367-375.

[28] Sun, C.T., Rui, Y., 1989. Orthotropic elasto-plastic behavior of AS4/APC-2 thermoplastic composite in compression. NASA CML 89-2.

[29] Rule, D.L., Sparks, L.L., 1989. Thermal conductivity of alumina fiber/epoxy and alumina fiber/PEEK from 4.2 to 310 K. Proceedings of the Twenty-First International Conference on Thermal Conductivity; October 15-18; Lexington, Kentucky.

[30] Jones, D.P., Leach, D.C., Moore, D.R., 1985. Mechanical properties of poly(ether-ether-ketone) for engineering applications. Polymer 26 (9), 1385-1393.

Appendix 1

The orthotropic stiffness matrix in material coordinates can be written in terms of engineering constants as:

$$[C] = \begin{bmatrix} C_{11} & C_{12} & C_{13} & 0 & 0 & 0 \\ C_{12} & C_{22} & C_{23} & 0 & 0 & 0 \\ C_{13} & C_{23} & C_{33} & 0 & 0 & 0 \\ 0 & 0 & 0 & C_{44} & 0 & 0 \\ 0 & 0 & 0 & 0 & C_{55} & 0 \\ 0 & 0 & 0 & 0 & 0 & C_{66} \end{bmatrix} = \begin{bmatrix} \frac{1}{E_1} & \frac{-\nu_{12}}{E_1} & \frac{-\nu_{13}}{E_1} & 0 & 0 & 0 \\ \frac{-\nu_{12}}{E_1} & \frac{1}{E_2} & \frac{-\nu_{23}}{E_2} & 0 & 0 & 0 \\ \frac{-\nu_{13}}{E_1} & \frac{-\nu_{23}}{E_2} & \frac{1}{E_3} & 0 & 0 & 0 \\ 0 & 0 & 0 & \frac{1}{G_{23}} & 0 & 0 \\ 0 & 0 & 0 & 0 & \frac{1}{G_{13}} & 0 \\ 0 & 0 & 0 & 0 & 0 & \frac{1}{G_{12}} \end{bmatrix}^{-1},$$

where subscripts 1, 2 and 3 refer to fibre longitudinal, transverse in-plane and out-of-plane directions respectively.

Layer off-axis stiffness constants are then transformed from constants along principal directions based on angle φ as follows [20]:

$$\{\bar{C}\}^{(k)} = [A]\{C\}^{(k)},$$

where:

$$\{\bar{C}\}^{(k)} = \left\{\bar{C}_{11}^{(k)}, \bar{C}_{12}^{(k)}, \bar{C}_{13}^{(k)}, \bar{C}_{16}^{(k)}, \bar{C}_{22}^{(k)}, \bar{C}_{23}^{(k)}, \bar{C}_{26}^{(k)}, \bar{C}_{33}^{(k)}, \bar{C}_{36}^{(k)}, \bar{C}_{44}^{(k)}, \bar{C}_{45}^{(k)}, \bar{C}_{55}^{(k)}, \bar{C}_{66}^{(k)}\right\}^T,$$

$$\{C\}^{(k)} = \left\{C_{11}^{(k)}, C_{22}^{(k)}, C_{33}^{(k)}, C_{12}^{(k)}, C_{13}^{(k)}, C_{23}^{(k)}, G_{23}^{(k)}, G_{12}^{(k)}, G_{13}^{(k)}\right\}^T.$$

The stiffness transformation matrix is:

Revision 28/1/2019 21:51
Deleted: 26

Revision 28/1/2019 21:51
Deleted: 27

Revision 28/1/2019 21:51
Deleted: 28

Revision 28/1/2019 21:51
Formatted: English (UK), Pattern: Clear (White)

Revision 28/1/2019 21:51
Deleted: [29

Revision 28/1/2019 21:51
Moved (insertion) [1]

Revision 28/1/2019 21:51
Deleted: Transformation matrix relating material and cylindrical axes: ... [51]

Revision 28/1/2019 21:51
Formatted: Indent: First line: 0 cm

Revision 28/1/2019 21:51
Moved (insertion) [2]

Revision 28/1/2019 21:51
Formatted: Font:Not Italic

Revision 28/1/2019 21:51
Formatted: Font:Not Italic

Revision 28/1/2019 21:51
Formatted: Font:Not Italic

Revision 28/1/2019 21:51
Moved (insertion) [3]

Revision 28/1/2019 21:51
Moved (insertion) [4]

Revision 28/1/2019 21:51
Moved (insertion) [5]

$$[A]=\begin{bmatrix} m^4 & n^4 & 0 & 2m^2n^2 & 0 & 0 & 0 & 0 & 4m^2n^2 \\ m^2n^2 & m^2n^2 & 0 & m^4+n^4 & 0 & 0 & 0 & 0 & -4m^2n^2 \\ 0 & 0 & 0 & 0 & m^2 & n^2 & 0 & 0 & 0 \\ m^3n & -mn^3 & 0 & -m^3n+mn^3 & 0 & 0 & 0 & 0 & -2m^3n+2mn^3 \\ n^4 & m^4 & 0 & 2m^2n^2 & 0 & 0 & 0 & 0 & 4m^2n^2 \\ 0 & 0 & 0 & 0 & n^2 & m^2 & 0 & 0 & 0 \\ mn^3 & -m^3n & 0 & m^3n-mn^3 & 0 & 0 & 0 & 0 & 2m^3n-2mn^3 \\ 0 & 0 & 1 & 0 & 0 & 0 & 0 & 0 & 0 \\ 0 & 0 & 0 & 0 & mn & -mn & 0 & 0 & 0 \\ 0 & 0 & 0 & 0 & 0 & 0 & m^2 & n^2 & 0 \\ 0 & 0 & 0 & 0 & 0 & 0 & -mn & mn & 0 \\ 0 & 0 & 0 & 0 & 0 & 0 & n^2 & m^2 & 0 \\ m^2n^2 & m^2n^2 & 0 & -2m^2n^2 & 0 & 0 & 0 & 0 & (m^2-n^2)^2 \end{bmatrix},$$

where $m = \cos\varphi$ and $n = \sin\varphi$.

Similarly, the expansion coefficients in principal coordinates can be transformed to the cylindrical axis for the thermal strains [14]:

$$\begin{Bmatrix} \alpha_z \\ \alpha_\theta \\ \alpha_r \\ \alpha_{z\theta} \end{Bmatrix}^{(k)} = \begin{bmatrix} m^2 & n^2 & 0 \\ n^2 & m^2 & 0 \\ 0 & 0 & 1 \\ mn & -mn & 0 \end{bmatrix} \begin{Bmatrix} \alpha_1 \\ \alpha_2 \\ \alpha_3 \end{Bmatrix}^{(k)}.$$

Revision 28/1/2019 21:51
Moved (insertion) [6]